iScience

Article

CryAB-driven amyloidogenesis in *Drosophila* muscle engages extracellular vesicle pathways for cellular release

Graphical abstract

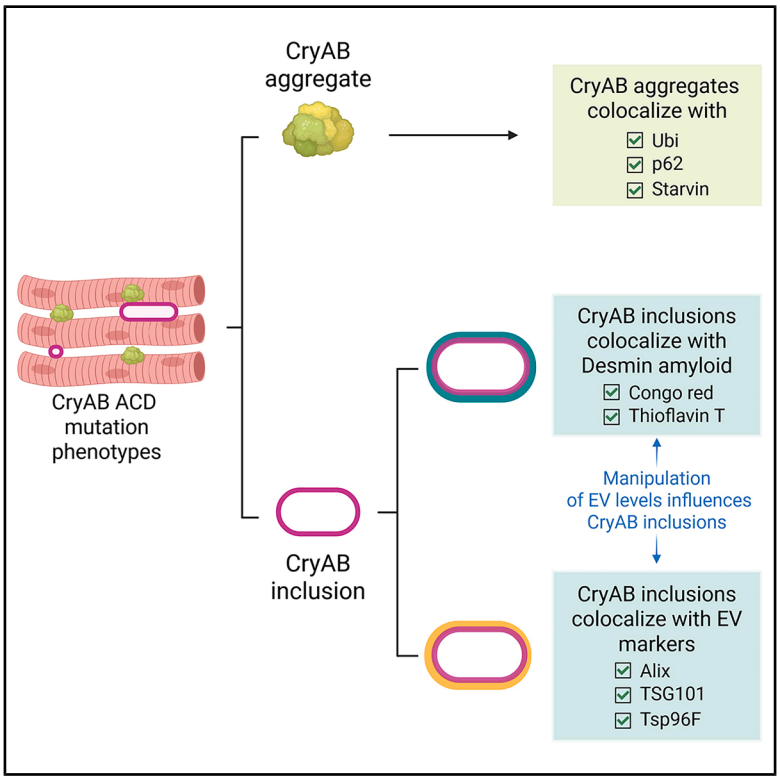

Highlights

- Human CryAB disease alleles promote protein aggregate accumulation in muscle
- CryAB mutations within the ACD domain form inclusions with amyloid characteristics
- Amyloid-like CryAB inclusions associate with a subset of EV proteins
- Amyloidogenic CryAB exists in muscles and is detected in the hemolymph

Authors

Ziwei Zhao, Hui-Ying Lim, Elena Cannone, ..., Zong-Heng Wang, Brian Glancy, Erika R. Geisbrecht

Correspondence

geisbrechte@ksu.edu

In brief

Biological sciences; Molecular biology; Neuroscience

Zhao et al., 2026, iScience *29*, 115461
April 17, 2026
https://doi.org/10.1016/j.isci.2026.115461

CellPress

iScience

CellPress
OPEN ACCESS

Article

CryAB-driven amyloidogenesis in *Drosophila* muscle engages extracellular vesicle pathways for cellular release

Ziwei Zhao,[1] Hui-Ying Lim,[2] Elena Cannone,[3] Giulia Marchetto,[4] Marco Schiavone,[3] Gaetano Vattemi,[4] Yungui Guo,[1] Zong-Heng Wang,[5] Brian Glancy,[5] and Erika R. Geisbrecht[1,6,*]

[1]Department of Biochemistry and Molecular Biophysics, Kansas State University, Manhattan, KS 66506, USA
[2]Department of Genetics, University of Alabama at Birmingham, Birmingham, AL 35294, USA
[3]Department of Molecular and Translational Medicine, Zebrafish Facility, University of Brescia, 25123 Brescia, Italy
[4]Department of Neurosciences, Biomedicine and Movement Sciences, University of Verona, 37129 Verona, Italy
[5]National Heart, Lung, and Blood Institute (NHLBI), National Institutes of Health, Bethesda, MD 20892, USA
[6]Lead contact
*Correspondence: geisbrechte@ksu.edu
https://doi.org/10.1016/j.isci.2026.115461

SUMMARY

Mutations in the small heat shock protein α-crystallin B (CryAB) result in cataracts, cardiomyopathies, and myofibrillar myopathies (MFMs), all of which are marked by protein aggregation. To investigate pathological mechanisms, we expressed four human CryAB disease alleles in *Drosophila* skeletal muscle. All variants resulted in the accumulation of protein aggregates. Mutations within the conserved α-crystallin domain (ACD) caused CryAB-positive structures that colocalized with an amyloidogenic form of human Desmin. The amyloid-like nature of these CryAB variants was further supported by thioflavin T spectroscopy and Congo red staining, the latter of which was also evident in other MFM-causing genes in zebrafish muscles and human biopsies. Muscle-enriched CryAB amyloid-like structures co-localized with extracellular vesicle (EV) markers and were detected in the hemolymph, suggesting an EV-mediated export mechanism. This is the first report of CryAB amyloid formation in skeletal muscle and broadens amyloid dynamics beyond the nervous system.

INTRODUCTION

Protein homeostasis, or proteostasis, is an equilibrium system that ensures proper protein folding and degradation. When proteostasis fails, protein aggregates with pathological roles may form, as seen with tau in Alzheimer's disease and alpha-synuclein in Parkinson's disease.[1–4] A hallmark of Alzheimer's and Parkinson's diseases is amyloid fiber formation in the brain.[5–7] However, this fibrillar-like protein aggregation, also known as amyloidosis, extends beyond neurodegenerative diseases—it can occur in the lungs, kidneys, muscles, and other organs.[8–11] However, it is yet unclear if other types of protein aggregates that form in non-neuronal tissues are linked to the formation of amyloid fibers.

Myofibrillar myopathies (MFMs) are a type of protein aggregate disease characterized by muscle fiber degeneration and progressive muscle weakness - typically in distal limb muscles.[12–15] Although MFMs can onset in early childhood, symptoms commonly appear later in life.[16] A subset of muscle proteins, including the Z-disk-associated proteins Desmin, Myotilin, Filamin C, α-Crystallin B (CryAB), and Bag3, is overrepresented and abnormally accumulates in biopsies from patients with MFM.[17–19] Due to the diversity of mutations in MFM-causing genes and the lack of understanding of the underlying pathogenicity of disease initiation and progression, there are no effective treatments.

To date, over 15 different mutations in CryAB have been linked to MFMs and/or cardiomyopathies.[20–25] CryAB, also known as heat shock protein 5 (HSPB5), is widely expressed across various tissues.[26] As a chaperone protein, CryAB aids in protein refolding and prevents aggregation. This approximately 20 kDa monomer forms highly ordered hetero-oligomeric complexes in response to intracellular stresses (heat, aging, oxidative or reductive stress) to sequester damaged or misfolded proteins, thereby maintaining proteostasis.[27,28] Mutations in CryAB lead to structural and functional changes that impair its interactions with client proteins, with distinct mutations producing varying effects on CryAB function. For instance, the D109A and R157H mutations differentially decrease or enhance chaperone activity *in vitro*, respectively.[29,30] Previous studies suggest that CryAB helps protect cytoskeletal myofibrils,[31] implying that mutant CryAB may play a pathological role in muscle and cardiac tissue.

Intercellular communication is essential for maintaining tissue homeostasis and coordinating physiological processes between tissues. One key mechanism by which cells communicate is through extracellular vesicles (EVs), which transport molecular signals - including proteins, lipids, and RNA - between cells.[32–35] Beyond their secretory role in normal physiology, EVs are also

widely implicated in pathological contexts, particularly in cancer, where they contribute to tumor growth, survival, and metastasis.[36–39] EV biogenesis involves a tightly regulated series of intracellular trafficking events. Early endosomes mature into multivesicular bodies (MVBs), which package selected cargos for eventual secretion. Once formed, MVBs can fuse with the plasma membrane, releasing their contents as EVs into the extracellular space using two primary routes: Endosomal sorting complex required for transport (ESCRT)-dependent and ESCRT-independent pathways.[40,41] While the role of EVs in cancer has been extensively studied, their involvement in muscle disorders, particularly in MFMs, remains largely unexplored. Given the progressive and sometimes systemic nature of MFM pathologies,[13,42] understanding the potential for EV-mediated protein clearance and/or disease propagation could reveal underlying mechanisms of pathogenesis.

Despite decades of research, the pathogenicity of CryAB mutations remains incompletely understood. Although numerous CryAB mutations have been identified, most research has focused on the R120G mutation, limiting a broader genotype-phenotype correlation.[20,43–49] To fill this scientific gap, we selected one pseudo-phosphorylation mutation (S70E) previously identified in our laboratory, along with four independent human CryAB mutations (R120G, D109A, D109H, and R157H) for further analysis using *Drosophila melanogaster (D. melanogaster)* as a cell biological model. R120 and D109A are causative for myofibrillar myopathy-2A (MFM2A, MIM: 608810), D109A is associated with MFM and multisystemic phenotypes,[29] while R157H is linked to patients with dilated cardiomyopathy (CMD1II, MIM: 615184).

First, we show that CryAB mutations disrupt protein homeostasis via impaired molecular chaperone activity, resulting in the accumulation of misfolded proteins marked by ubiquitin (Ubi) and the autophagy adaptor protein p62/SQSTM1. Second, we identify CryAB intracellular structures that are amyloidogenic in nature. Mutations in CryAB exhibit amyloid-like properties not only in *Drosophila* muscle, but also in zebrafish and human MFM muscle biopsies, potentially indicating a conserved and clinically relevant pathogenic feature. Third, we observe that CryAB amyloid-like structures can exit muscle cells by engaging the EV pathway. This connection between amyloid formation and EV dynamics provides a potential mechanism for amyloid clearance and transport *in vivo*. In summary, this study establishes a mechanistic link between CryAB mutations, amyloid formation, and EV-mediated export from muscle tissue, possibly as a protective mechanism to limit tissue damage. Our findings extend the role of CryAB beyond protein quality control, highlighting its broader impact on cytoskeletal dynamics, vesicle trafficking, and disease progression.

RESULTS

CryAB is comprised of an alpha-crystallin domain (ACD) common to heat shock family proteins and less conserved flexible N- and C-terminal regions that are responsible for oligomerization and the binding of client proteins.[26,28] Primary amino acid sequence alignments show that the location of the dominant human CryAB mutations D109, R120, and R157 are conserved in *Drosophila* (D113, R124, and R163), although we will continue to use the human amino acid numbering here (Figure S1A). Residues D109 and R120 reside within the ACD, while R157 is positioned near the C-terminus (Figure 1A). *In vitro* studies demonstrate that the CryAB mutations D109A and R120G induce oligomerization, while R157H does not, suggesting that the location of each mutation distinctly influences the structural and functional properties of CryAB.[25,26]

To investigate the *in vivo* effects of each CryAB mutation, we generated transgenic *Drosophila* lines expressing four conserved human mutations (D109A, D109H, R120G, R157H) and wild-type CryAB under the control of upstream activating sequences (UASs). Each of these CryAB pathogenic alleles was independently expressed under the control of the *Myocyte enhancer factor 2* (*Mef2*) promoter.[50,51] For phenotypic analysis, we first examined wandering third-instar larvae (L3), whose larger size facilitates easy muscle dissection and imaging. L3 carcasses were stained with anti-CryAB and phalloidin to assess protein distribution and muscle structure, respectively. While F-actin striations appeared normal, the sarcomeric CryAB protein pattern was disrupted, instead forming distinct circular or oval structures upon the expression of ACD mutations (D109A, D109H, and R120G) (Figure 1B, open white arrowheads). We previously identified two residues in CryAB (S68 and S70) that are phosphorylated by the NUAK serine/threonine (S/T) kinase.[52] The location of these phosphorylated residues is conserved in the human CryAB sequence (Figure S1A), but as of yet, no human mutations are linked to disease. Only the S70A or S70E mutations displayed a CryAB phenotype similar to the ACD variants (Figures 1B and S1B). Since S70 is located within the ACD (Figure 1A), we collectively refer to D109A, D109H, R120G, and S70E as "ACD domain mutations."

Aging is characterized by the accumulation of cellular damage, contributing to functional decline and heightened disease susceptibility.[53] Human mutations in CryAB promote protein accumulation with age in specific tissues, namely the eye, brain, and heart.[26,54,55] To investigate if human CryAB mutations affect *Drosophila* lifespan, we monitored the longevity of transgenic flies at 31°C. As shown in Figure 1C, overexpression of either wildtype or mutant CryAB significantly shortened lifespan compared to *mCh RNAi* controls ($p < 0.0001$), with wildtype CryAB exhibiting 50% lethality around day 15. No statistically significant lethality was observed in the pupal stage compared to *mCh* controls (Figure S1C). These findings demonstrate that increased temperature exacerbates CryAB-associated toxicity and negatively affects the longevity of *Drosophila*.

Since CryAB mutations can cause dilated cardiomyopathies (DCMs),[26,27,30,56] we next investigated how CryAB mutations affect protein aggregation and structural abnormalities in this tissue. First, we verified that all CryAB insertion lines driven by *Mef2*-Gal4 expressed similar amounts of CryAB protein since they were all inserted into the same attB site on chromosome 2 (Figures S1D and S1E). Next, we selected D109A and R120G for heart tube staining. Immunostaining revealed excess or irregular CryAB distribution (Figure S1F, open arrowheads) compared to normal Z-disc localization (Figure S1F, open arrows). We also detected numerous Ubi-positive puncta, suggesting the formation of protein aggregates within the heart tube

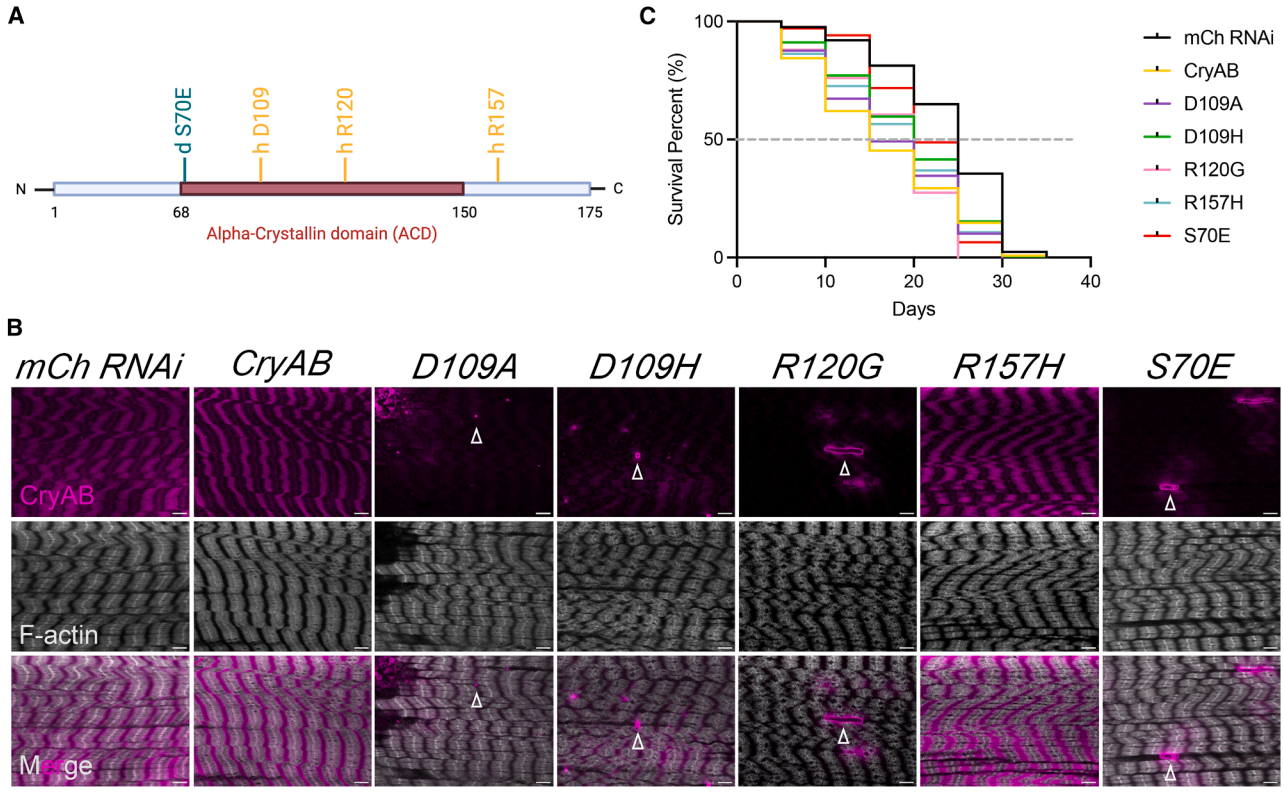

Figure 1. Impacts of CryAB mutations on protein localization in *Drosophila*

Also see Figure S1.

(A) Schematic of CryAB domains. The flexible N-terminal domain is involved in oligomer assembly, the conserved alpha-crystallin domain (ACD) is required for dimer formation, and the C-terminal domain is associated with hexamer formation. The location of the mutations being analyzed is shown.

(B) Confocal images of L3 muscles expressing the *mCh RNAi* and wild-type *CryAB* (*CryAB*) controls along with the indicated *CryAB* point mutations. All UAS constructs are driven using *Mef2*-Gal4. F-actin is shown in gray and CryAB in magenta. Aberrant CryAB structures are indicated by the open white arrowheads. Scale bars, 5 μm.

(C) Survival curves of adult flies expressing *CryAB* variants. While *mCh RNAi* controls show extended longevity, expression of wild-type *CryAB* and *CryAB* mutants significantly reduces lifespan, with over 50% mortality in the *WT* group by day 15 (n = 3 biological replicates, $N \geq 50$ for each genotype, Simple survival analysis, Kaplan-Meier). $p < 0.0001$.

(Figure S1F, solid arrowheads). Due to the small size and limited resolution of the heart tube, these phenotypes were difficult to assess in detail. To overcome this limitation, we shifted our focus to the indirect flight muscles (IFMs), which offer the advantage of larger tissue size and more muscle fibers for clearer observations of morphological and pathological changes.

CryAB mutations promote insoluble aggregates

Given the role of CryAB mutations in diseases that disrupt protein turnover, we investigated whether these pathogenic alleles lead to protein aggregation in the IFMs. Based upon our lifespan analysis (Figure 1C), we selected days 2 and 10 females flies to ensure we had enough viable adults for experiments to assess the impact of *CryAB* mutations during this 8-day period of mild aging. Confocal microscopy revealed two distinct phenotypes in the IFMs: aggregates and inclusions (Figure 2A and Video S1). CryAB aggregates, defined as solid CryAB immunostaining that overlapped with Ubi signal, were present in all genotypes tested. In contrast, all CryAB ACD domain mutations, but not *CryAB WT* or *R157H*, also revealed hollow, circular structures that stained positive for CryAB, which we have termed CryAB inclusions. Here we present evidence supporting each of these phenotypes.

We first used Ubi to label misfolded and/or aggregated proteins that fail to undergo degradation. Co-staining with CryAB antibodies confirmed more Ubi accumulation in IFMs expressing CryAB ACD domain mutations at day 2 (Figure 2B). Quantitative analysis of Ubi aggregates using ImageJ confirmed that D109A, R120G, and S70E exhibited a significant increase in Ubi aggregates - at least 2-fold higher than CryAB or R157H at day 2 (Figure 2C). However, by day 10, aggregates marked by Ubi were observed in all genotypes, with the largest increase in D109H and R120G (Figures 2D and S2A). Colocalization analysis revealed that CryAB ACD domain mutations exhibited more than a 60% increase in CryAB/Ubi overlap compared to CryAB or R157H at day 2, with a continuous increase in the aggregation of all genotypes by day 10 (Figure 2E).

The observed accumulation of CryAB aggregates in muscle tissue is characteristic of protein aggregation and predicts that these complexes may lead to protein insolubility. To confirm the presence of insoluble CryAB, we performed western blot

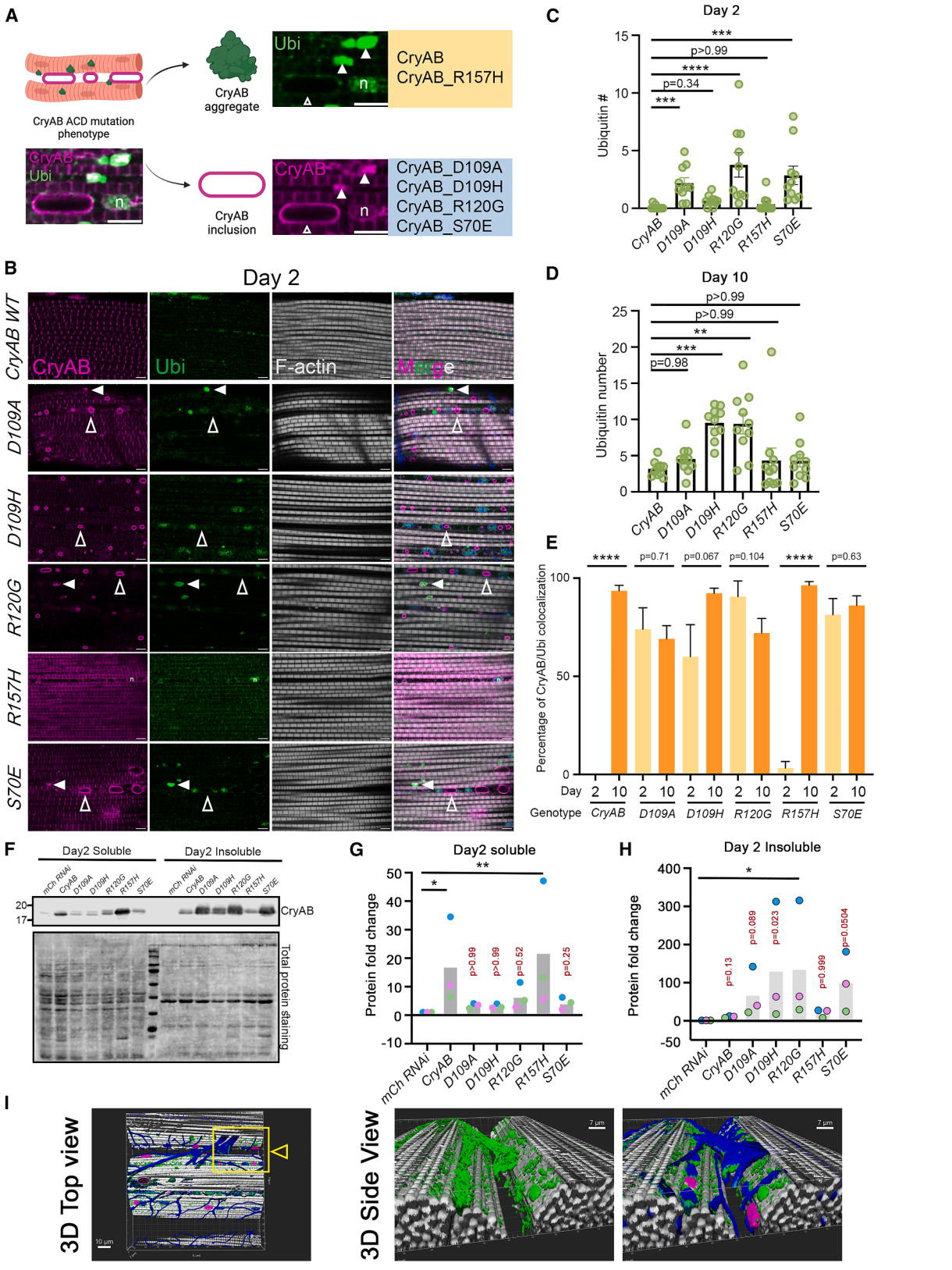

(legend on next page)

analysis. CryAB and R157H were markedly enhanced in the soluble pool of CryAB at days 2 and 10 (Figures 2F, 2G, S2B, and S2C). In contrast, mutations within the ACD domain showed elevated levels of CryAB protein in the insoluble fraction compared to the *mCh* control at both timepoints, while only R120G or S70E met the threshold for statistical significance (Figures 2F–2H, S2B, and S2D). Overall, these observations show that ACD domain mutations promote CryAB insolubility, which is an indicator of protein aggregation. 3D imaging further supported the presence of CryAB aggregates, revealing circular structures with varying intensities of Ubi staining in IFMs expressing R120G (Figure 2I).

Proteins destined for degradation in the lysosome via autophagy or by the proteasome can both be tagged with Ubi.[57] To establish which aspect(s) of proteostasis may be altered by CryAB mutations, we next examined the localization and levels of the autophagy adaptor protein p62/SQSTM1 (Sequestosome 1), which marks ubiquitinated cargo proteins.[58] Immunostaining showed colocalization of Ubi aggregates with p62 (Figure S3A, solid arrowheads). Western blot analysis and protein quantification did not show a significant increase in insoluble p62 protein levels, although R120G displayed an upward trend (Figures S3B–S3D). These observations indicate that while p62 colocalizes with Ubi-positive aggregates, CryAB mutations do not measurably impair autophagic flux. However, days 2 and 10 IFMs expressing mutant CryAB proteins showed a reduction in proteasome activity (Figures S4A and S4B). These data together show that CryAB mutations do not overtly disrupt autophagic turnover, but fail to upregulate proteasome function, thereby promoting the progressive accumulation of aggregates with age in muscle tissue.

Since the BAG-domain-containing co-chaperone protein Starvin (Stv) also marks aggregates[59] and is required for autophagic protein degradation,[60,61] we next examined Stv localization. Indeed, Stv labeled Ubi aggregates in the IFMs (Figure S4C, solid arrowheads). Note that not all aggregates were degraded via Bag3-related autophagy since some Ubi aggregates did not co-localize with Stv (Figure S4C, asterisks). Here, we conclude that protein aggregates, marked by CryAB, Ubi, p62, and Stv, accumulate with age in *Drosophila* IFMs, accompanied by decreased proteosome activity upon the expression of CryAB mutant proteins.

CryAB ACD mutations promote inclusion formation

As previously mentioned, we observed a distinct phenotype characterized by hollow circular or oval structures outlined by CryAB staining prevalent in both L3 larval muscles (Figure 1B, open arrowheads) and adult IFMs (Figure 2B, open arrowheads). The lack of colocalization with Ubi or p62 indicated that CryAB inclusions were not associated with canonical proteasome or autophagy protein degradation pathways. To further characterize these CryAB inclusions, we conducted statistical analyses on the number and size of these structures across different mutations and ages. All CryAB ACD mutations (D109A, D109H, R120G, and S70E), but not CryAB or R157H, showed significantly more inclusions in both days 2 and 10 IFMs (Figures 3A and 3B). We also observed size variation, leading to the hypothesis that inclusion size would increase with age. Indeed, while only an increase in the size of D109A and S70E inclusions was statistically significantly from days 2 to 10, other ACD mutations exhibited a strong trend of inclusion size growth (Figure 3C).

To gain further insight into the composition of CryAB inclusions, we performed transmission electron microscopy (TEM) on two CryAB ACD mutations (D109A and S70E) to analyze the IFM ultrastructure. Low-magnification micrographs (1500×) revealed the embedding of inclusion-like structures between myofibrils without significantly disrupting tissue integrity (Figures 3D–3F). Higher magnification TEM images (5000×) surprisingly showed inclusions as large structures surrounding multiple smaller inclusions in D109A (Figure 3E) or S70E (Figure 3F, top panel) muscles. This internal structural complexity was only occasionally visible using immunofluorescence, likely due to limited antibody penetration. Notably, fibril-like structures were also observed in S70E (Figure 3F, bottom panel). Increased magnification (8000×) revealed detailed, irregular ribbon-like formations that eventually looped to form protofilament-like structures. These findings provide *in vivo* evidence that CryAB mutations may promote structures similar to amyloid-like architecture.

CryAB inclusions co-localize with amyloidogenic Desmin and exhibit amyloid features

Desmin-related myopathy (DRM) or myofibrillar myopathy 1 (MFM1, MIM: 601419) is characterized by myofibrillar dissolution and the accumulation of the intermediate filament protein

Figure 2. CryAB mutations disrupt proteostasis and promote insoluble aggregates

Also see Figures S2–S4 and Video S1.

(A) Schematic summarizing the two phenotypes observed in adult IFMs: aggregation (CryAB co-localized with Ubi, solid white arrowheads) and inclusions (CryAB staining without Ubi, open white arrowheads). CryAB inclusions are associated with mutations in the ACD domain (*D109A, D109H, R120G, S70E*). Scale bars, 5 μm.

(B) Representative images of day 2 adult IFMs show F-actin (gray), CryAB (magenta), and Ubi (green). *CryAB WT* and *R157H* exhibit Z-disc localization, while ACD mutations display aggregates and inclusions. Nuclei are counterstained with Hoechst (blue). Scale bars, 5 μm.

(C and D) Quantification of Ubi-positive aggregates in days 2 and 10 flies is represented as a scatter bar plot. Data are mean ± SEM ($N = 10$ per genotype, Kruskal-Wallis test). $^{**}p < 0.01$, $^{***}p < 0.001$, and $^{****}p < 0.0001$.

(E) Percentage of CryAB/Ubi colocalization in aggregates of days 2 and 10 IFMs. Data are mean ± SEM ($N = 10$ per genotype, Mann-Whitney test). $^{****}p < 0.0001$.

(F) Western blot shows soluble and insoluble CryAB levels in day 2 adult samples. ACD mutations result in increased insoluble CryAB compared to Cry WT and R157H. Total protein staining serves as a loading control. $n \geq 3$.

(G and H) Bar graph shows the quantification of soluble and insoluble CryAB protein from (F). Data are mean ± SD (n = 3, Kruskal-Wallis test). $^{*}p < 0.05$ and $^{**}p < 0.01$.

(I) Three-dimensional (3D) confocal rendering of IFMs expressing R120G. IFMs are labeled for F-actin (gray), Ubi (green), CryAB (magenta), and nuclei with Hoechst (blue). The yellow box in the top-view image (left) was used to generate side views (right). Non-specific Hoechst signal marks tracheal tissue. Scale bars, 10 μm for top view image and 7 μm for side view images.

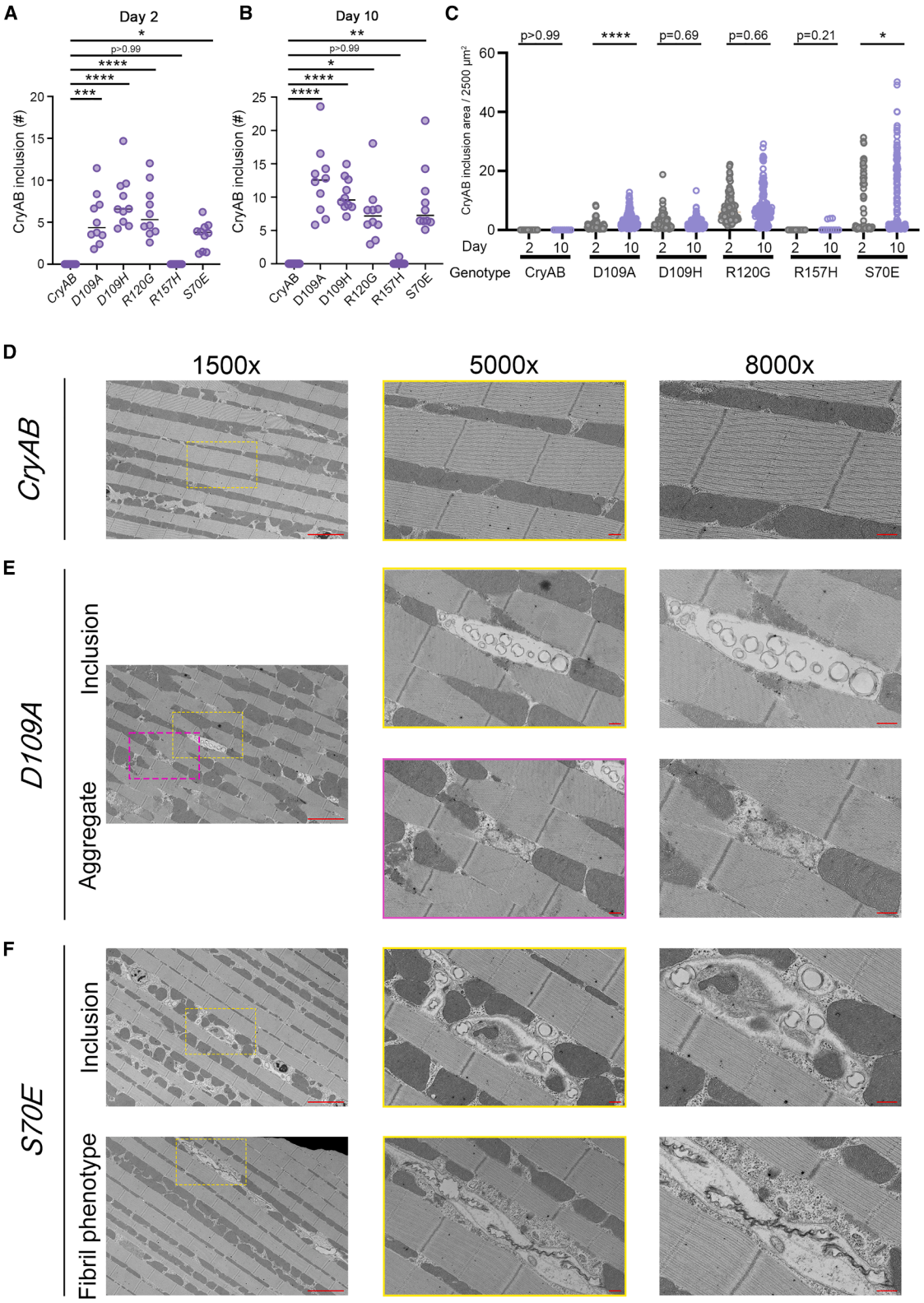

(legend on next page)

Desmin.[62] Moreover, *in vitro* studies showed that CryAB R120G can induce Desmin aggregation.[63,64] To test if an amyloidogenic region (aa 117–348) of Desmin[65] possesses *in vivo* amyloid-like features similar to CryAB, we developed a humanized model of DRM (Figure 4A). The expression of amyloidogenic human Desmin revealed Desmin-positive inclusions that overlapped with CryAB staining (Figure 4B, open arrowheads). Co-expression of CryAB ACD mutations also co-localized with amyloidogenic Desmin (Figure 4C, open arrowheads), further supporting the amyloid-like nature of CryAB inclusions. Occasionally, small inclusions were also present with CryAB alone or R157H when co-expressed with hDesmin, suggesting that normal or heightened chaperone activity was insufficient to prevent the amyloid phenotype induced by human Desmin. Quantitative analysis confirmed that the number of CryAB(+) inclusions in flies co-expressing amyloidogenic Desmin along with CryAB mutations were not significantly different from those with Desmin alone at day 2 or 10 (Figures S5A–S5C).

To further substantiate the amyloid-like nature of our CryAB(+) inclusions, we isolated them from muscle tissue (Figure 5A) and stained with the amyloid marker Congo red. Extracted inclusions from muscles expressing D109A, R120G, or S70E all stained positive for Congo red and CryAB (Figures 5B and S5D). Isolation of these inclusions allowed for improved reagent penetration as we were able to detect smaller circular structures inside the typical CryAB(+) staining (Figure S5D), similar to those seen by TEM (Figures 3E and 3F). To further confirm the amyloid-like nature of CryAB inclusions, we used the amyloid-sensitive fluorescent dye Thioflavin T (ThT). Samples were subjected to sequential centrifugation to enrich for the inclusion-containing fraction (Figure 5A). Increasing volumes of CryAB-containing fractions showed a proportional rise in ThT fluorescence, consistent with the presence of amyloid structures (Figure 5C). The D109A mutant showed a statistically significant increase in fluorescence intensity at 100 μL compared with wild-type CryAB, while the R120G mutant exhibited an even stronger response, with significantly elevated ThT signal detectable at volumes as low as 25 μL. Together, the Congo red labeling experiments and ThT assays demonstrate that CryAB inclusions contain amyloid-like architecture.

CryAB amyloid-like inclusions are present in zebrafish and human muscle

Next, we wanted to test whether amyloid-like aggregates can form in muscle tissue from other species expressing human mutations. We first assessed *hCryAB G154S* since this mutation causes MFM, but not cataracts or cardiomyopathy.[66,67] Compared to *hCryAB WT*, *hCryAB G154S* expression resulted in approximately a 40% increase in Congo red staining (Figures 6A and 6B), confirming the presence of amyloid-like aggregates in zebrafish muscle. Next, we investigated whether similar amyloid features could be observed with other proteins implicated in MFMs. We focused on human *Myotilin* (*MYOT*), another gene commonly mutated in patients with MFM.[68] Zebrafish embryos injected with *hMYOT S95I* displayed a 50% occurrence of Congo red-positive aggregates, approximately 20% higher than *hMYOT WT* (Figures 6C and 6D). These results demonstrate that amyloid accumulation is not restricted to CryAB mutations in *Drosophila* but is a broader pathological feature in vertebrate muscles.

To extend these findings to human pathology, we analyzed muscle biopsy samples from patients with MFM carrying mutations in *CryAB* (G154S), *MYOT* (S60F), or *Desmin* (R454W). In all cases, histological examination revealed features characteristic of MFMs, including variable fiber size and fatty replacement assessed by hematoxylin and eosin (H&E) and NADH-tetrazolium reductase (NADH-TR) staining (Figures 6E–6G). Importantly, these patient tissues also showed positive Congo red staining, reinforcing the presence of amyloid-like structures. Collectively, these data suggest that amyloid accumulation is a shared pathological feature across multiple MFM-related genes and model systems. This supports a broader hypothesis that amyloidogenesis is not limited to neurodegenerative conditions, but may also be a central mechanism in muscle diseases such as MFMs.

Intersection of CryAB inclusions and EV involvement

TEM analysis and confocal microscopy identified multiple examples of CryAB amyloid-like structures either on the surface of muscle fibers (Figure 7A) or just outside the muscle boundary (Figure 7B, open yellow arrowhead; Video S2). These data posited that these structures may be transported or released from muscle tissue. To test this possibility, we isolated EV-enriched fractions from the hemolymph of thoraces using differential centrifugation (Figure 7C). CryAB assemblies were detected in the hemolymph and stained positive for Congo red, reaffirming their amyloid-like properties (Figure 7D). To rule out contamination from hemocytes or other nucleated cells, we included Hoechst staining. The absence of the Hoechst signal confirmed that the isolated material consisted of cell-free CryAB inclusions (Figure 7D). Together, these results demonstrate that CryAB amyloid-like structures can exit muscle tissue into the extracellular space.

To explore the mechanism behind this secretion, we performed mass spectrometry (MS) to compare the proteomes of inclusions isolated from CryAB and D109A hemolymph. The D109A inclusions (compared to CryAB) showed marked proteomic changes, with 199 proteins enriched ($\log_2$ abundance ratio ≥ 1, $p \leq 0.05$) and 58 reduced ($\log_2$ abundance ratio ≤ -1, $p \leq 0.05$) relative to wild-type CryAB (Table S1). Gene Ontology (GO) analysis of the enriched proteins revealed strong overrepresentation of pathways related to exosomal secretion, lysosomal organization, and endosomal vesicle fusion

Figure 3. Overexpression of CryAB ACD mutations promotes inclusion formation

(A and B) Quantification of CryAB inclusions per genotype in day 2 IFMs. Data are mean ($N = 10$ per genotype, Kruskal-Wallis test). *$p < 0.05$, **$p < 0.01$, ***$p < 0.001$, and ****$p < 0.0001$.

(C) Inclusion area per 2500 μm^2 for days 2 and 10 IFMs. Data are median ($N = 10$ per genotype, Mann-Whitney test). *$p < 0.05$ and ***$p < 0.001$.

(D–F) TEM analysis of day 10 IFMs across genotypes. D109A shows aggregates and inclusions, while S70E exhibits aggregate-inclusion transitions and fibril-like structures. Magnifications: 1500× scale bars, 5 μm, 5000× scale bars, 500 nm, and 8000× scale bars, 500 nm.

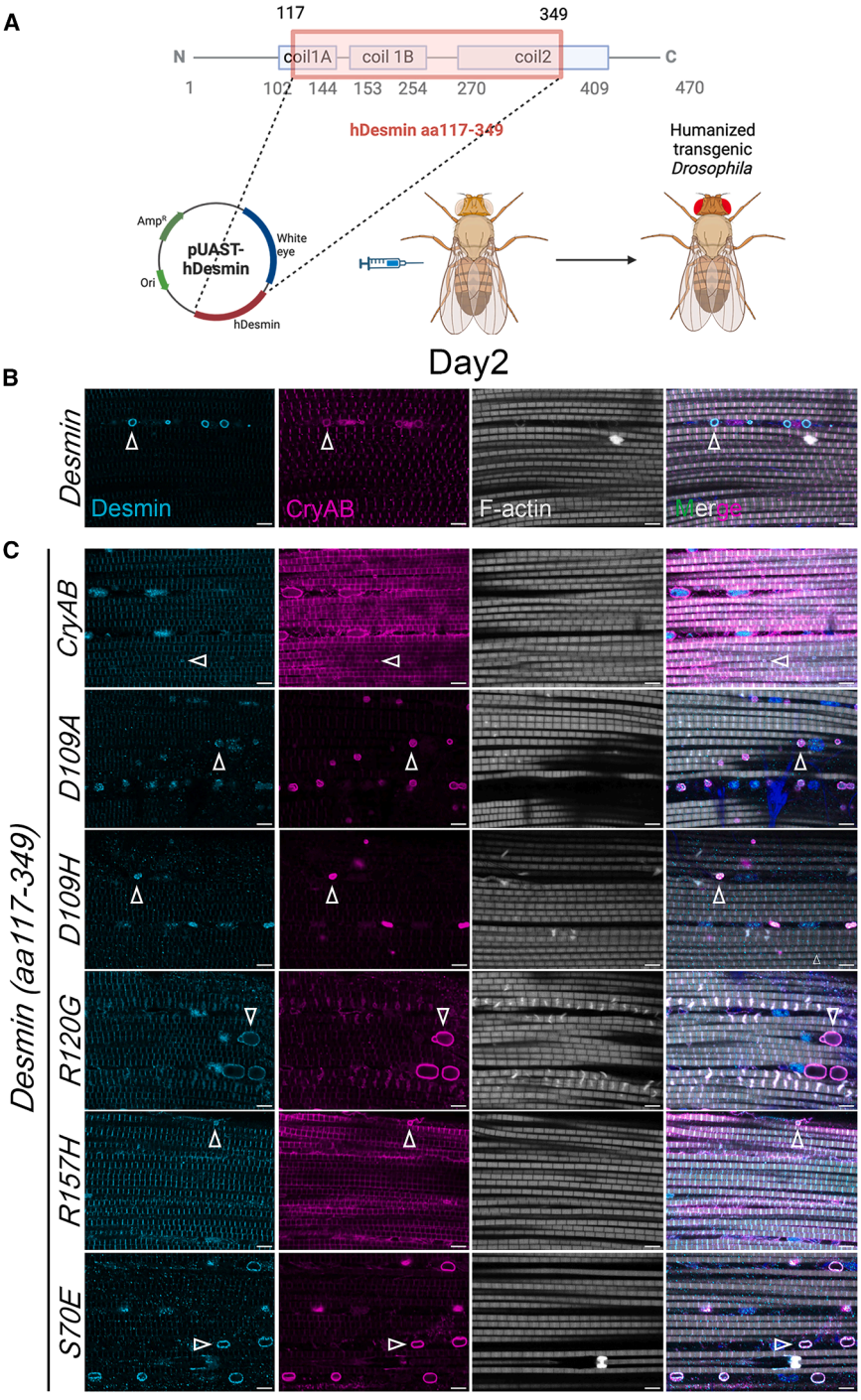

Figure 4. An amyloidogenic form of hDesmin phenocopies CryAB inclusion accumulation

Also see Figure S5.

(A) Schematic of the amyloidogenic region of Desmin (AA 117–349) used to generate humanized Desmin transgenic fly lines.

(B and C) Immunostaining of IFMs with *Mef2*-Gal4 expressing *hDesmin* (AA 117–349) alone (B) or with *CryAB* mutants (C). hDesmin (cyan) forms structures similar to CryAB inclusions (open white arrowheads) in day 2 IFMs. F-actin is labeled in gray and nuclei are stained with Hoechst (blue). Scale bars, 5 μm.

(Figure 7E). Notably, several regulators of vesicle trafficking - including the ESCRT accessory protein ALG-2 interacting protein X (Alix), the endosomal fusion protein Rab7, and the exosomal marker Tetraspanin 42Ee (Tsp42Ee) - were significantly elevated in the D109A sample (Figure 7F). These findings show that markers for EV pathways are associated with CryAB amyloid-like inclusions that have been released into the hemolymph from the IFMs.

Next, we explored the *in vivo* connection between EV proteins and CryAB amyloid-like structures using immunofluorescence and genetic approaches. We first focused on Alix and Rab7 as they were enriched in our MS dataset. Co-expression of *Alix-HA* with *CryAB* mutants, but not *CryAB WT*, showed robust colocalization between Alix-HA and CryAB inclusions (Figure 7G). Quantification revealed that Alix overexpression significantly increased both the area and number of inclusions in the D109A and R120G mutants (Figures 7H and 7I). Consistent with the enrichment of Rab7 in our D109A MS experiments, indeed, Rab7 immunostaining overlapped with CryAB inclusions (Figure S6A). Since Alix is defined as an ESCRT-associated protein,[40,41] we also examined Tumor susceptibility gene 101 (TSG101), a core ESCRT-I component, and observed similar colocalization with CryAB structures (Figure S6B). The same trend held true for Rab27 (Figure S6C), the ortholog of mammalian Rab27 A/B, which is implicated in EV biogenesis and secretion.[69] These results suggest the possibility that the biogenesis and/or release of CryAB amyloid-like structures may involve ESCRT and endosomal trafficking pathways.

Although Tsp42Ee, the human homolog of CD63, emerged in our MS data, no antibody or tagged version exists to examine colocalization with CryAB. Therefore, we tested whether a human CD63 transgenic (UAS-hCD63-GFP) line could serve as a surrogate marker. Human CD63 did not colocalize with CryAB amyloid-like inclusions, suggesting that the human protein does not function properly in the *Drosophila* context (Figure S6E). This lack of colocalization provided a useful negative control for assessing the specificity of CryAB amyloid-like structures. Other proteins that might be predicted to colocalize

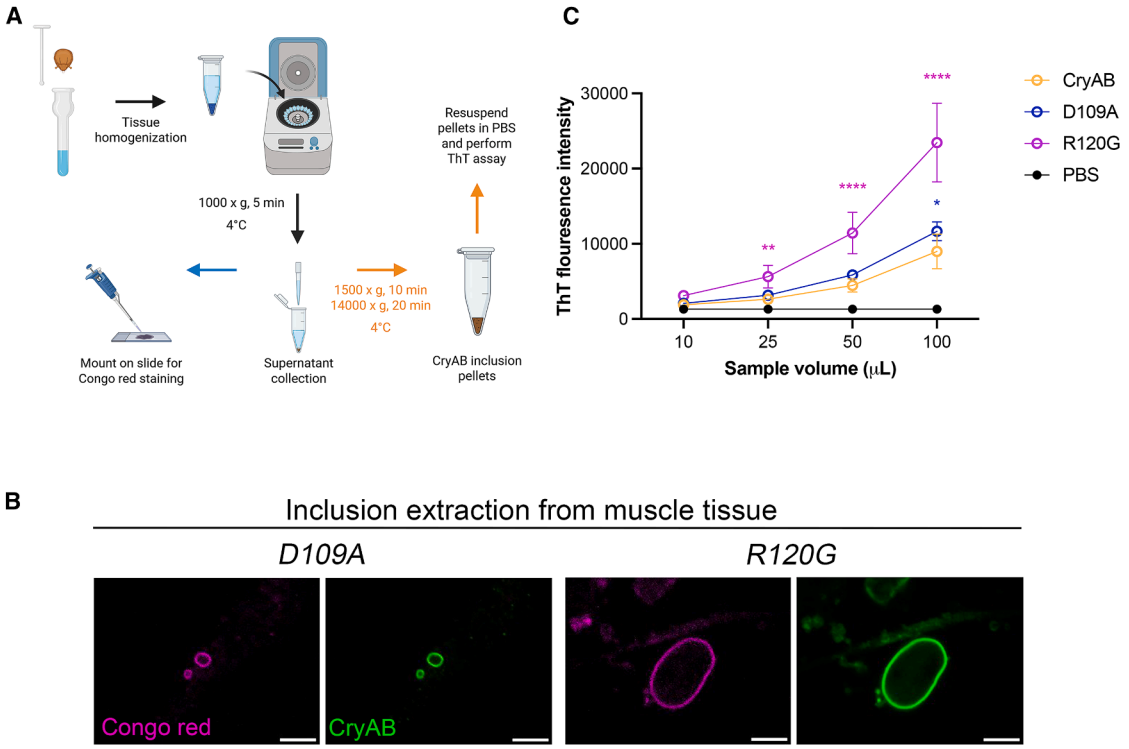

Figure 5. Extraction of muscle CryAB inclusions and characterization of amyloid features

(A) Schematic overview of the workflow used to isolate CryAB-containing inclusions from adult IFMs.

(B) CryAB inclusions purified from adult IFMs and stained with Congo red. Immunofluorescence using an anti-CryAB antibody (green) shows clear colocalization with Congo red-positive structures (magenta), indicating amyloid fibril-like properties. Scale bars, 5 μm.

(C) Thioflavin T (ThT) fluorescence assay used to detect and quantify amyloid-like structures across increasing volumes of CryAB-containing muscle lysate. $N = 6$ for each sample. Mean and error ± SD (two-way ANOVA with Dunnett's multiple comparisons test). $^{**}p < 0.01$, $^{***}p < 0.001$, and $^{****}p < 0.0001$.

with CryAB inclusions based on a role in endosome trafficking (Rab5) or the propensity to form amyloid (human alpha-synuclein, SNCA) were also tested. However, neither one of these proteins colocalized with CryAB inclusions (Figures S6F and S6G). Combined with yeast two-hybrid data whereby mutant CryAB exhibited stronger binding to its interacting protein NUAK than to CryAB WT (Figures S7A and S7B), it is clear that mutant CryAB does not simply associate with any abundant protein. Instead, our results support the selective association between CryAB inclusions and specific EV proteins, highlighting a targeted mechanism for their trafficking and potential extracellular release.

Mechanisms of EV secretion vary depending on cargos and can be classified into ESCRT-independent or -dependent pathways.[40,70,71] Because our MS results did not highlight proteins associated with ESCRT-independent cargo sorting, we chose to examine Tetraspanin 96F (Tsp96F), the *Drosophila* homolog of the mammalian EV marker CD81, as a representative protein of this pathway.[72] Expression of Tsp96F tagged with mCherry (*mCh-Tsp96F*) in the IFMs showed a diffuse pattern while CryAB maintained its normal Z-disc location (Figure 8A). To assess the effect of Tsp96F on CryAB inclusion dynamics, we co-expressed *mCh-Tsp96F* with either *D109A* or *R120G* at 25°C. In both cases, Tsp96F colocalized with CryAB inclusions (Figures 8A and 8B, open arrowheads). Quantitation revealed that overexpression of *Tsp96F* significantly increased the size of CryAB inclusions (Figure 8C), while the number of inclusions increased only for D109A (Figure 8D). Conversely, RNAi-mediated knockdown of *Tsp96F* led to a marked reduction in inclusion size for both D109A and R120G at 31°C (Figures 8E–8G), while only D109A showed a decrease in inclusion number (Figure 8H). These data together indicate that modulating the protein levels of Tsp96F or Alix (Figures 7H and 7I) is sufficient to increase or decrease the formation and size of CryAB-inclusions.

DISCUSSION

This study investigated the tissue-level consequences of human CryAB disease alleles (D109A, D109H, R120G, and R157H) using a *Drosophila* model to explore their pathological effects in striated muscle tissue. While all CryAB mutations increased the amount of Ubi-marked protein aggregates, only ACD domain mutations caused the accumulation of amyloidogenic structures. These *in vivo* results are consistent with previous observations that D109 mutations possess amyloid-forming properties *in vitro*.[29,56] The disruption of amino acid interactions in the ACD region, primarily composed of beta sheet secondary structures, is crucial to this process. Each CryAB monomer interacts via antiparallel beta strands 6 and 7 located in the ACD, where

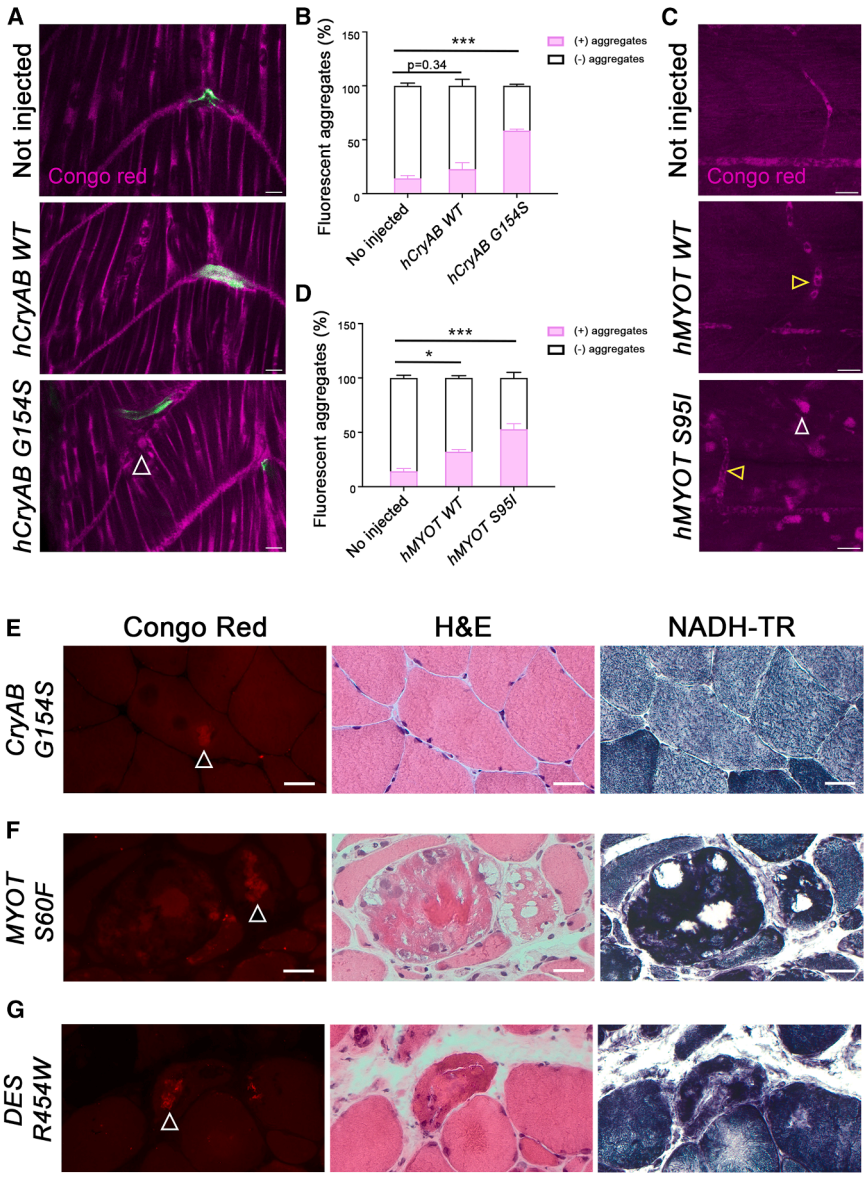

Figure 6. ACD domain mutations induce amyloid deposition in zebrafish and are associated with congophilic inclusions in human MFMs

(A) Representative images of whole-mount Congo red staining in zebrafish embryos at 120 h post-fertilization (hpf). Embryos were either uninjected, injected with human wild-type *CRYAB* (*hCRYAB WT*), or with the G154S mutant (*hCRYAB G154S*). Merged images show Congo red staining (magenta) and vasculature labeled by the tg(*kdrl:EGFP*) transgene (green). Open white arrows highlight congophilic aggregates in trunk muscle fibers. $N = 3$ independent experiments. Scale bars, 5 μm.

(B) Bar graph quantification of embryos exhibiting Congo red-positive aggregates. Not injected (5/35), *hCRYAB WT* (7/29), *hCRYAB G154S* (31/53). Mean ± SEM. (One-way ANOVA with Bonferroni correction). ***$p < 0.001$.

(C) Congo red staining of zebrafish embryos injected with human *MYOT* constructs. Embryos were either uninjected or injected with wild-type (*hMYOT WT*) or mutant (*hMYOT S95I*) forms. White arrows indicate Congo red-positive deposits in muscle fibers. Open yellow arrows indicate intersomitic blood vessels. $N = 3$ independent experiments. Scale bars, 20 μm.

(D) Bar graph quantification of embryos with Congo red-positive aggregates. Not injected (5/35), *hMYOT WT* (10/31), *hMYOT S95I* (11/21). Mean ± SEM. (One-way ANOVA with Bonferroni correction). *$p < 0.05$ and ***$p < 0.001$.

(E–G) Histological analysis of skeletal muscle from patients with MFM. Congo red staining (left) reveals fluorescent amyloid deposits (red) in muscle fibers from (E) a patient with the *CRYAB* p.Gly154Ser mutation, (F) a patient with the *MYOT* p.Ser60Phe mutation, and (G) a patient with the *DES* p.Arg454Trp mutation. Corresponding H&E (middle) and NADH (right) stains highlight structural abnormalities. Images were captured using a 40× objective. Scale bars, 100 μm.

both D109 and R120 are positioned to form ionic bonds for dimerization.[29,73] These mutations decrease the stability of oligomers and may lead to unfolding of normally stable beta sheets. Such destabilization would predict a higher propensity to spuriously interact with other proteins to form aggregates and/or amyloidogenic structures, thus leading to a more stable oligomeric structure that resists degradation by autophagy or proteases.

There was a definitive increase in inclusion number and a trend of larger inclusion size upon the expression of CryAB mutations. CryAB inclusions might reach a maximal size due to space constraints within the tissue. Another possibility is that inclusion size might increase with age, which could not be fully assessed in this model due to a shortened lifespan upon the expression of CryAB mutations. While both *CryAB WT* or the *R157H* mutations were associated with age-related lethality similar to those in the ACD domain (possibly due to altered cardiac function), these alleles did not promote amyloid fiber formation *in vivo*. *In vitro*, the R157H mutation enhances the chaperone activity of CryAB,[30] which is also observed in patients undergoing chemotherapy where CryAB expression is elevated.[74] This suggests that heightened chaperone function, while cytoprotective, may actually be harmful under certain conditions.

Our interest in CryAB originated from its identification as a substrate for the NUAK S/T kinase, where we identified two conserved phosphorylation sites (S68 and S70) in CryAB.[75] The S70E and S70A mutations show an amyloid-like phenotype similar to the ACD mutations D109 and R120. Despite literature that CryAB phosphorylation regulates extracellular secretion,[76] the lack of phenotypic differences between phospho-null and phospho-mimetic changes at amino acid S70 suggests that its location within the ACD domain, and not its phosphorylation

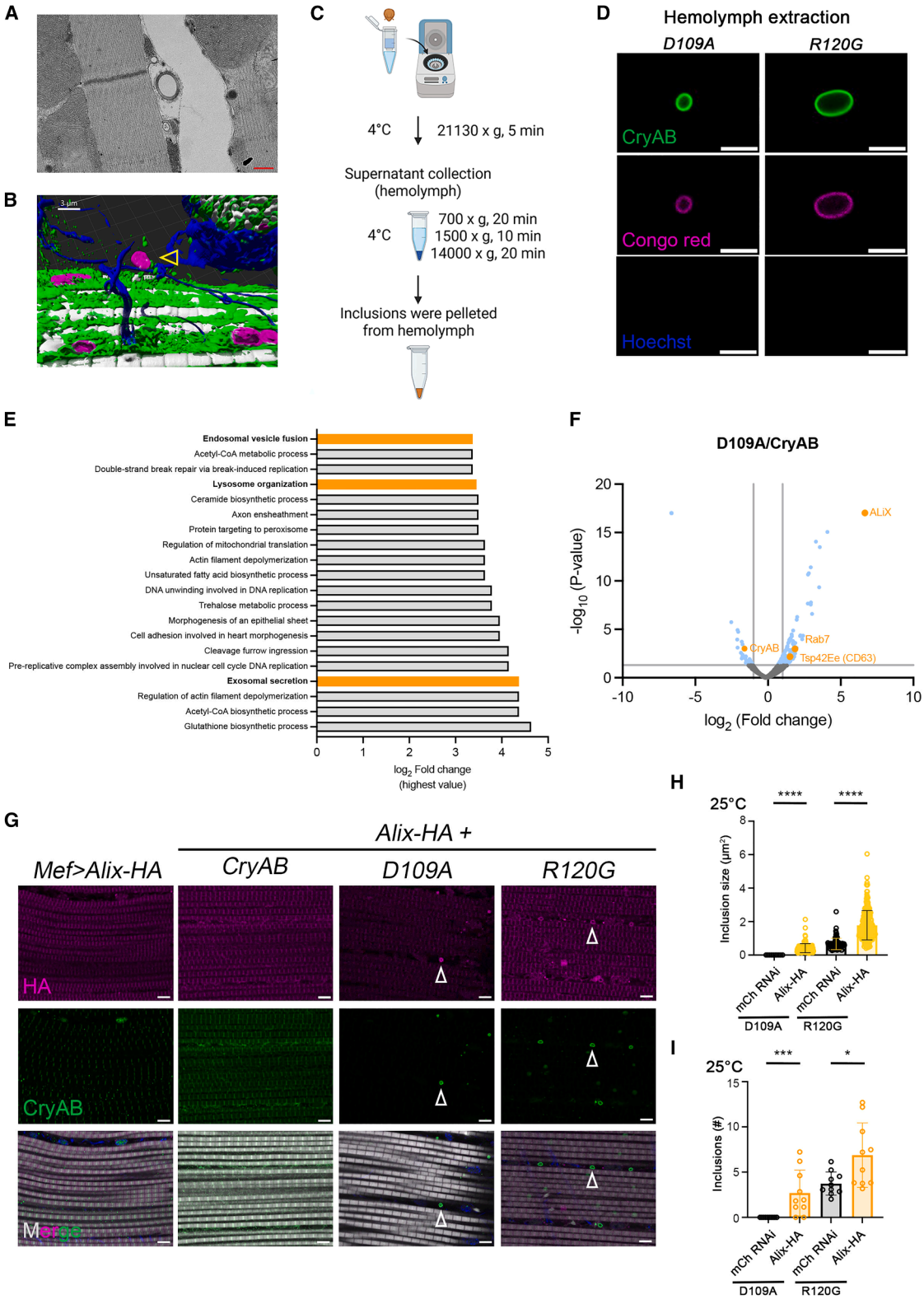

(legend on next page)

status, promotes amyloid formation. To further explore how CryAB may impact other aspects of NUAK-mediated signaling, we conducted immunoprecipitation experiments with 3×-HA-tagged CryAB to identify proteins in muscle lysates that physically bind to CryAB. Unfortunately, cell lysis resulted in the pull-down of hundreds of interacting proteins, suggesting that CryAB is a promiscuous binding protein in non-cellular contexts. Switching to yeast two-hybrid assays, we confirmed that CryAB mutants exhibit higher binding affinity with NUAK under selective pressure (0.5–3 mM 3-AT), supporting previous findings that mutant CryAB forms stable complexes with client proteins, hindering degradation.

Although amyloid fibrils are predominantly studied in the brain, amyloid deposition in skeletal muscle is poorly understood. The presence of CryAB inclusions containing amyloid-like architecture was suggested by TEM images, colocalization with an amyloidogenic region of hDesmin, and further validated with positive Congo red and ThT fluorescence. Observing such clear protofibril structures by TEM was unexpected, as *in vivo* amyloid deposition can be challenging to detect due to its small size. Since amyloid fibrils are typically markers of a progressive disease,[6,7] the shorter longevity of our animal model may have precluded observations of fibril accumulation. To our benefit, the Gal4-mediated *in vivo* expression system "enriched" for aggregates and amyloid inclusions, likely due to higher expression levels of mutant CryAB proteins. The ability to modulate CryAB mutant expression by raising the temperature to increase output of the Gal4/UAS system at the same time may have introduced *in vivo* heat stress to further promote amyloid formation. These inherent advantages likely promoted CryAB amyloid formation compared to the normal intracellular environment, which prevents spontaneous fibril formation.

While *in vitro* studies provide valuable insights into amyloid microstructures, they lack a comprehensive understanding of amyloid macroscopic architecture in living organisms. A meaningful example of this is the presence of circular amyloid structures in muscle, likely forming due to space and tension constraints implicit in a contractile tissue such as muscle. The mechanical properties of these fibrils, capable of forming annular amyloid *in vitro* due to bending and stretching abilities, align with previous reports on amyloid flexibility.[77–79] In addition to our findings in *Drosophila*, we validated the presence of amyloid aggregates in both zebrafish and human patient CryAB muscle samples. These results confirm that CryAB-related amyloidogenic structures are not species-specific and likely represent a conserved mechanism of muscle pathology.[67] The consistent detection of amyloid-like aggregates across models in our work and others[14,80] suggests that amyloid-specific staining, such as Congo red, holds promise as a diagnostic tool in muscle diseases, particularly in MFMs.

Importantly, we identified a link between CryAB inclusions and EV pathways, suggesting that CryAB amyloids are secreted as a protective mechanism since they cannot be degraded via normal degradation pathways. This expands the scope of amyloid biology beyond the nervous system to include muscle tissue. In the future, small-molecule drugs targeting CryAB mutations could potentially prevent amyloid fibril formation by disrupting these stable oligomeric structures. Our ongoing research will focus on identifying the precise molecular mechanisms and protein interactions that facilitate CryAB amyloid fibril formation *in vivo*. Understanding these pathways could shed light on amyloid deposition processes in muscle tissue and their parallels with neurodegenerative diseases.

Limitations of the study

While this study establishes conserved amyloid-like features of CryAB mutations across multiple model systems, some limitations should be acknowledged. First, the *Drosophila* Gal4/UAS system promotes elevated expression levels of mutant CryAB proteins *in vivo*, which may accelerate aggregate formation compared to normal aging or disease conditions. The shortened lifespan of flies expressing CryAB mutations also limited our ability to evaluate long-term age-dependent progression and maximal inclusion size. Second, while amyloid architecture was validated using TEM, Congo red, and ThT, the structural resolution remains below that of cryo-EM, preventing definitive assignment of fibril polymorphs or molecular packing. Finally, although the EV-associated secretion of CryAB inclusions was supported by genetic and biochemical evidence, direct visualization of CryAB-loaded vesicle trafficking *in vivo* will require higher-resolution live imaging or correlative EM approaches.

Figure 7. CryAB inclusions are released from muscle tissue and associate with EV proteins

Also see Figures S6 and S7, Video S2, and Table S1.

(A) TEM images of day 10 IFMs expressing the D109A mutation reveal inclusions on the surface of muscle tissue. Magnification: 5000× scale bar, 500 nm.

(B) 3D rendering of IFMs expressing R120G. Mitochondria are labeled with ATP5α (green), CryAB inclusions are shown in magenta, F-actin in gray, and nuclei with Hoechst (blue). Non-specific Hoechst signal marks tracheal tissue. Yellow open arrowhead indicates CryAB inclusion located outside of muscle. Scale bars, 3 μm.

(C) A schematic of the protocol used for EV extraction from thorax hemolymph.

(D) CryAB inclusions isolated from thoracic hemolymph. CryAB is shown in green, Congo red-stained amyloid in magenta, and Hoechst in blue to identify nuclei and exclude hemocytes. Scale bars, 5 μm.

(E) Gene Ontology (GO) analysis of biological processes resulting from D109A/CryAB MS experiments shows the enrichment of proteins in pathways associated with vesicle formation, intracellular trafficking, and secretion.

(F) Volcano plot of proteins identified in MS experiments plotted to assess proteins enriched in mutant CryAB (D109A) compared to controls (CryAB). Proteins with a significance value of $p \leq 0.05$ are in blue. EV proteins enriched in CryAB mutant inclusions that are labeled in orange ($\log_2$ abundance ratio ≥ 1). Note that more peptides corresponding to CryAB were detected in controls, hence the $\log_2$ abundance ratio ≤ 1. $n = 3$ biological replicates.

(G) Colocalization analysis of CryAB amyloid-like structures with the EV marker Alix. Flies co-expressing HA-tagged Alix (Alix-HA) and mutant CryAB proteins under control of the *Mef2* driver were raised at 25°C and dissected at day 2. CryAB (green) colocalizes with HA (magenta) in IFMs. Scale bars, 5 μm.

(H and I) Scatter bar plot quantification of CryAB inclusion size (H) and number (I) in IFMs co-expressing Alix at day 2. Data are presented as mean ± SD. ($N = 10$ per genotype, Mann-Whitney test). $^{*}p < 0.05$, $^{***}p < 0.001$, and $^{****}p < 0.0001$.

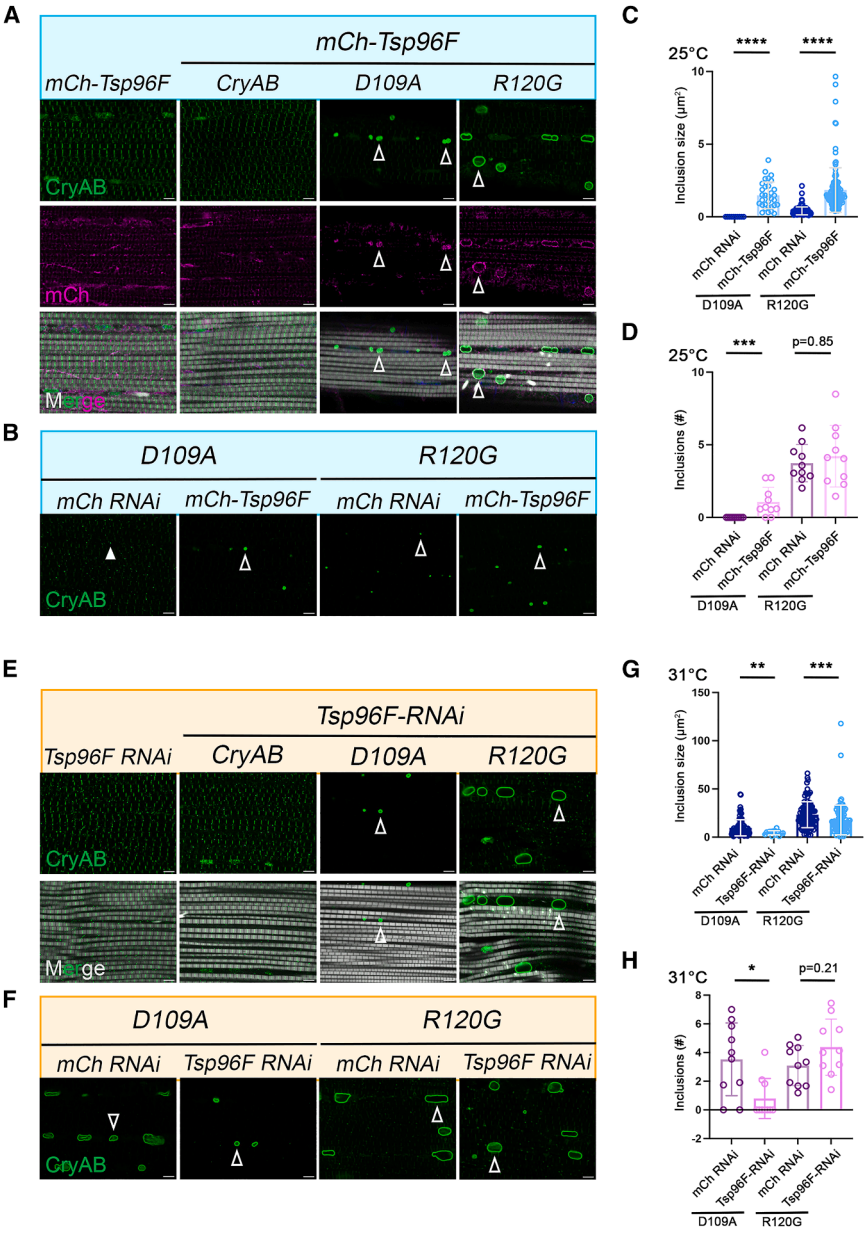

Figure 8. Colocalization of CryAB amyloid-like inclusions with EV markers and quantification of inclusion phenotypes

Also see Figures S6 and S7.

(A) Flies co-expressing mCherry-tagged Tsp96f (*mCh-Tsp96f*) and mutant *CryAB* variants under control of the *Mef2*-Gal4 driver were raised at 25°C and dissected at day 2. CryAB (green) shows clear colocalization with *Tsp96f* (magenta) in IFMs, highlighted with white open arrowheads. Scale bar, 5 µm.

(B) Representative images used for quantification in (C) and (D). D109A or R120G (green, white open arrowheads) co-expressed with *mCh RNAi* controls or *mCh-Tsp96f*. White arrowhead indicates small CryAB-positive puncta that fall below the defined measurement threshold.

(C and D) Scatter bar plots quantifying CryAB inclusion size (C) and number (D) in IFMs co-expressing *Tsp96f* at day 2. Data are presented as mean ± SD (n = 10 per genotype, Mann-Whitney test). ***$p < 0.001$ and ****$p < 0.0001$.

(E) Representative single-plane IFM images from day 2 adult flies following *Tsp96f RNAi* induction at 31°C. CryAB is shown in green and F-actin in gray. Scale bars, 5 µm.

(F) Sample quantification images for (G) and (H), based on CryAB antibody staining (green, white open arrowheads). D109A or R120G co-expressed with *mCh RNAi* served as controls for quantification.

(G and H) Scatter bar plots quantifying CryAB inclusion size (G) and number (H) in IFMs upon *Tsp96f RNAi* induction. Data are presented as mean ± SD (n = 10 per genotype, Mann-Whitney test). *$p < 0.05$, **$p < 0.01$, and ***$p < 0.001$.

RESOURCE AVAILABILITY

Lead contact

Further information and requests for resources and reagents should be directed to and will be fulfilled by the lead contact, Erika R. Geisbrecht (geisbrechte@ksu.edu).

Materials availability

For any reasonable requests regarding materials produced in this study, please contact the lead contact.

Data and code availability

- Data availability - All data are included in the manuscript and associated supplements. The MS proteomics data have been deposited at MassIVE under accession code MSV000100788 and at ProteomeXchange as PXD074306 and are publicly available at https://doi.org/10.25345/C5ZK5611C.
- Code availability - This paper does not report original code.
- All other data availability - Any additional information required to reanalyze the data reported in this paper is available from the lead contact upon request.

ACKNOWLEDGMENTS

We thank Huiquan Duan for assistance with preparing L-lysine-coated slides. A special thanks to Larysa Stroganova at the University of Kansas Medical Center for her excellent assistance with our TEM studies and Zachary Clark, Michaella Rekowski, and Michael Washburn at the University of Kansas Medical Center for their excellent assistance and expediency with our MS analysis. We also thank Emma Peters and David Brooks for technical assistance and Jocelyn McDonald for discussion and insight. We are grateful to Dr. Julia Gross

for the *UAS-mCh-Tsp96f* flies and to Dr. Young Kwon for the *UAS-hCD63* flies. Schematics were created with BioRender.com.

This study was supported by the National Institute of Arthritis and Musculoskeletal and Skin Diseases of the National Institutes of Health under award number RO1AR060788 and the USDA National Institute of Food and Agriculture Hatch NC1184 project to E.R.G. Stocks obtained from the Bloomington *Drosophila* Stock Center (NIH P40OD018537) were used in this study. Thanks to the Kansas State University (KSU) Johnson Cancer Research Center (JCRC), KSU College of Arts & Sciences, the Reeck Graduate Travel Award, and the KSU Graduate Student Council (GSA) for travel funds to Z.Z. and Y.G.

AUTHOR CONTRIBUTIONS

Conceptualization, Z.Z. and E.R.G.; investigation, Z.Z., H.-Y.L., E.C., G.M., and Y.G.; primary data analysis, Z.Z., H.-Y.L., M.S., G.V., Y.G., and E.R.G.; image analysis, Z.-H.W.; writing and editing, Z.Z. and E.R.G.; resources Z.Z., funding acquisition, E.R.G.; supervision E.R.G.

DECLARATION OF INTERESTS

The authors declare no competing interests.

STAR★METHODS

Detailed methods are provided in the online version of this paper and include the following:

- KEY RESOURCES TABLE
- EXPERIMENTAL MODEL AND STUDY PARTICIPANT DETAILS
  - *Drosophila* stocks and husbandry
  - Zebrafish maintenance
  - Human muscle biopsy collection
- METHOD DETAILS
  - Creation of transgenic flies
  - Visualization of muscle tissue
  - Western blotting to assess soluble and insoluble fractions
  - Lethal stage analysis
  - Quantification of CryAB aggregates or inclusions
  - Transmission Electron Microscopy (TEM)
  - CryAB inclusion extraction from muscle
  - Congo red and CryAB staining
  - Thioflavin T (ThT) assay
  - Hemolymph inclusion extraction
  - Mass spectrometry
  - Proteasome activity assay
  - Yeast two-hybrid (Y2H)
  - Zebrafish Congo red staining
  - Human biopsy histochemistry
- QUANTIFICATION AND STATISTICAL ANALYSIS

SUPPLEMENTAL INFORMATION

Supplemental information can be found online at https://doi.org/10.1016/j.isci.2026.115461.

Received: August 18, 2025
Revised: December 19, 2025
Accepted: March 19, 2026
Published: March 21, 2026

REFERENCES

1. Almeida, C.G., Takahashi, R.H., and Gouras, G.K. (2006). β-amyloid accumulation impairs multivesicular body sorting by inhibiting the ubiquitin-proteasome system. J. Neurosci. *26*, 4277–4288.
2. Freer, R., Sormanni, P., Vecchi, G., Ciryam, P., Dobson, C.M., and Vendruscolo, M. (2016). A protein homeostasis signature in healthy brains recapitulates tissue vulnerability to Alzheimer's disease. Sci. Adv. *2*, e1600947.
3. Cheng, J., North, B.J., Zhang, T., Dai, X., Tao, K., Guo, J., and Wei, W. (2018). The emerging roles of protein homeostasis-governing pathways in Alzheimer's disease. Aging Cell *17*, e12801.
4. Xilouri, M., Brekk, O.R., and Stefanis, L. (2013). Alpha-synuclein and protein degradation systems: a reciprocal relationship. Mol. Neurobiol. *47*, 537–551.
5. Braak, H., and Braak, E. (1991). Demonstration of amyloid deposits and neurofibrillary changes in whole brain sections. Brain Pathol. *1*, 213–216.
6. Hayashi, H., Kimura, N., Yamaguchi, H., Hasegawa, K., Yokoseki, T., Shibata, M., Yamamoto, N., Michikawa, M., Yoshikawa, Y., Terao, K., et al. (2004). A seed for Alzheimer amyloid in the brain. J. Neurosci. *24*, 4894–4902.
7. Rodrigue, K.M., Kennedy, K.M., and Park, D.C. (2009). Beta-amyloid deposition and the aging brain. Neuropsychol. Rev. *19*, 436–450.
8. Kyle, K.A., and BAYED, K.D. (1975). Amyloidosis: review op 236 cases. Medicine *54*, 271–299.
9. Hazenberg, B.P.C. (2013). Amyloidosis: a clinical overview. Rheum. Dis. Clin. North Am. *39*, 323–345.
10. Wechalekar, A.D., Gillmore, J.D., and Hawkins, P.N. (2016). Systemic amyloidosis. Lancet *387*, 2641–2654.
11. Benson, M.D., Buxbaum, J.N., Eisenberg, D.S., Merlini, G., Saraiva, M.J.M., Sekijima, Y., Sipe, J.D., and Westermark, P. (2020). Amyloid nomenclature 2020: update and recommendations by the International Society of Amyloidosis (ISA) nomenclature committee. Amyloid *27*, 217–222. https://doi.org/10.1080/13506129.2020.1835263.
12. Nakano, S., Engel, A.G., Waclawik, A.J., Emslie-Smith, A.M., and Busis, N.A. (1996). Myofibrillar myopathy with abnormal foci of desmin positivity. I. Light and electron microscopy analysis of 10 cases. J. Neuropathol. Exp. Neurol. *55*, 549–562.
13. Schröder, R., and Schoser, B. (2009). Myofibrillar myopathies: a clinical and myopathological guide. Brain Pathol. *19*, 483–492.
14. Selcen, D., and Engel, A.G. (2011). Myofibrillar myopathies. Handb. Clin. Neurol. *101*, 143–154.
15. Claeys, K.G., and Fardeau, M. (2013). Myofibrillar myopathies. Handb. Clin. Neurol. *113*, 1337–1342.
16. Olivé, M., Odgerel, Z., Martínez, A., Poza, J.J., Bragado, F.G., Zabalza, R.J., Jericó, I., Gonzalez-Mera, L., Shatunov, A., Lee, H.S., et al. (2011). Clinical and myopathological evaluation of early-and late-onset subtypes of myofibrillar myopathy. Neuromuscul. Disord. *21*, 533–542.
17. Kley, R.A., Maerkens, A., Leber, Y., Theis, V., Schreiner, A., van der Ven, P.F.M., Uszkoreit, J., Stephan, C., Eulitz, S., Euler, N., et al. (2013). A combined laser microdissection and mass spectrometry approach reveals new disease relevant proteins accumulating in aggregates of filaminopathy patients. Mol. Cell. Proteomics *12*, 215–227. https://doi.org/10.1074/mcp.M112.023176.
18. Maerkens, A., Olivé, M., Schreiner, A., Feldkirchner, S., Schessl, J., Uszkoreit, J., Barkovits, K., Güttsches, A.K., Theis, V., Eisenacher, M., et al. (2016). New insights into the protein aggregation pathology in myotilinopathy by combined proteomic and immunolocalization analyses. Acta Neuropathol. Commun. *4*, 8. https://doi.org/10.1186/s40478-016-0280-0.
19. Maerkens, A., Kley, R.A., Olivé, M., Theis, V., van der Ven, P.F.M., Reimann, J., Milting, H., Schreiner, A., Uszkoreit, J., Eisenacher, M., et al. (2013). Differential proteomic analysis of abnormal intramyoplasmic aggregates in desminopathy. J. Proteomics *90*, 14–27. https://doi.org/10.1016/j.jprot.2013.04.026.
20. Vicart, P., Caron, A., Guicheney, P., Li, Z., Prévost, M.C., Faure, A., Chateau, D., Chapon, F., Tomé, F., Dupret, J.M., et al. (1998). A missense mutation in the alphaB-crystallin chaperone gene causes a desmin-related myopathy. Nat. Genet. *20*, 92–95. https://doi.org/10.1038/1765.

21. Sacconi, S., Féasson, L., Antoine, J.C., Pécheux, C., Bernard, R., Cobo, A.M., Casarin, A., Salviati, L., Desnuelle, C., and Urtizberea, A. (2012). A novel CRYAB mutation resulting in multisystemic disease. Neuromuscul. Disord. *22*, 66–72. https://doi.org/10.1016/j.nmd.2011.07.004.

22. Fichna, J.P., Potulska-Chromik, A., Miszta, P., Redowicz, M.J., Kaminska, A.M., Zekanowski, C., and Filipek, S. (2017). A novel dominant D109A CRYAB mutation in a family with myofibrillar myopathy affects αB-crystallin structure. BBA Clin. *7*, 1–7. https://doi.org/10.1016/j.bbacli.2016.11.004.

23. Inagaki, N., Hayashi, T., Arimura, T., Koga, Y., Takahashi, M., Shibata, H., Teraoka, K., Chikamori, T., Yamashina, A., and Kimura, A. (2006). αB-crystallin mutation in dilated cardiomyopathy. Biochem. Biophys. Res. Commun. *342*, 379–386.

24. Pilotto, A., Marziliano, N., Pasotti, M., Grasso, M., Costante, A.M., and Arbustini, E. (2006). alphaB-crystallin mutation in dilated cardiomyopathies: low prevalence in a consecutive series of 200 unrelated probands. Biochem. Biophys. Res. Commun. *346*, 1115–1117. https://doi.org/10.1016/j.bbrc.2006.05.203.

25. Thorkelsson, A., and Chin, M.T. (2024). Role of the Alpha-B-crystallin protein in cardiomyopathic disease. Int. J. Mol. Sci. *25*, 2826.

26. Dimauro, I., Antonioni, A., Mercatelli, N., and Caporossi, D. (2018). The role of αB-crystallin in skeletal and cardiac muscle tissues. Cell Stress Chaperones *23*, 491–505. https://doi.org/10.1007/s12192-017-0866-x.

27. Bakthisaran, R., Akula, K.K., Tangirala, R., and Rao, C.M. (2016). Phosphorylation of αB-crystallin: Role in stress, aging and patho-physiological conditions. Biochim. Biophys. Acta *1860*, 167–182. https://doi.org/10.1016/j.bbagen.2015.09.017.

28. Dimauro, I., and Caporossi, D. (2022). Alpha B-Crystallin in Muscle Disease Prevention: The Role of Physical Activity. Molecules *27*, 1147. https://doi.org/10.3390/molecules27031147.

29. Fichna, J.P., Potulska-Chromik, A., Miszta, P., Redowicz, M.J., Kaminska, A.M., Zekanowski, C., and Filipek, S. (2017). A novel dominant D109A CRYAB mutation in a family with myofibrillar myopathy affects αB-crystallin structure. BBA Clin. *7*, 1–7.

30. Nasiri, P., Ghahramani, M., Tavaf, Z., Niazi, A., Moosavi-Movahedi, A.A., Kurganov, B.I., and Yousefi, R. (2021). The biochemical association between R157H mutation in human αB-crystallin and development of cardiomyopathy: Structural and functional analyses of the mutant protein. Biochimie *190*, 36–49. https://doi.org/10.1016/j.biochi.2021.06.019.

31. Yin, B., Tang, S., Xu, J., Sun, J., Zhang, X., Li, Y., and Bao, E. (2019). CRYAB protects cardiomyocytes against heat stress by preventing caspase-mediated apoptosis and reducing F-actin aggregation. Cell Stress Chaperones *24*, 59–68.

32. Yáñez-Mó, M., Siljander, P.R.M., Andreu, Z., Zavec, A.B., Borràs, F.E., Buzas, E.I., Buzas, K., Casal, E., Cappello, F., Carvalho, J., et al. (2015). Biological properties of extracellular vesicles and their physiological functions. J. Extracell. Vesicles *4*, 27066. https://doi.org/10.3402/jev.v4.27066.

33. Yáñez-Mó, M., Siljander, P.R.-M., Andreu, Z., Zavec, A.B., Borràs, F.E., Buzas, E.I., Buzas, K., Casal, E., Cappello, F., Carvalho, J., et al. (2015). Biological properties of extracellular vesicles and their physiological functions. J. Extracell. Vesicles *4*, 27066.

34. Tkach, M., and Théry, C. (2016). Communication by extracellular vesicles: where we are and where we need to go. Cell *164*, 1226–1232.

35. Van Niel, G., d'Angelo, G., and Raposo, G. (2018). Shedding light on the cell biology of extracellular vesicles. Nat. Rev. Mol. Cell Biol. *19*, 213–228.

36. El Andaloussi, S., Mäger, I., Breakefield, X.O., and Wood, M.J.A. (2013). Extracellular vesicles: biology and emerging therapeutic opportunities. Nat. Rev. Drug Discov. *12*, 347–357.

37. Yamamoto, S., Azuma, E., Muramatsu, M., Hamashima, T., Ishii, Y., and Sasahara, M. (2016). Significance of extracellular vesicles: pathobiological roles in disease. Cell Struct. Funct. *41*, 137–143.

38. Xu, R., Rai, A., Chen, M., Suwakulsiri, W., Greening, D.W., and Simpson, R.J. (2018). Extracellular vesicles in cancer—implications for future improvements in cancer care. Nat. Rev. Clin. Oncol. *15*, 617–638.

39. Kalluri, R., and McAndrews, K.M. (2023). The role of extracellular vesicles in cancer. Cell *186*, 1610–1626.

40. Juan, T., and Fürthauer, M. (2018). Biogenesis and Function of ESCRT-dependent Extracellular Vesicles (Elsevier), pp. 66–77.

41. Vietri, M., Radulovic, M., and Stenmark, H. (2020). The many functions of ESCRTs. Nat. Rev. Mol. Cell Biol. *21*, 25–42. https://doi.org/10.1038/s41580-019-0177-4.

42. Luo, Y.B., Peng, Y., Lu, Y., Li, Q., Duan, H., Bi, F., and Yang, H. (2020). Expanding the Clinico-Genetic Spectrum of Myofibrillar Myopathy: Experience From a Chinese Neuromuscular Center. Front. Neurol. *11*, 1014. https://doi.org/10.3389/fneur.2020.01014.

43. Bova, M.P., Yaron, O., Huang, Q., Ding, L., Haley, D.A., Stewart, P.L., and Horwitz, J. (1999). Mutation R120G in alphaB-crystallin, which is linked to a desmin-related myopathy, results in an irregular structure and defective chaperone-like function. Proc. Natl. Acad. Sci. USA *96*, 6137–6142.

44. Wang, X., Osinska, H., Klevitsky, R., Gerdes, A.M., Nieman, M., Lorenz, J., Hewett, T., and Robbins, J. (2001). Expression of R120G–αB-crystallin causes aberrant desmin and αB-crystallin aggregation and cardiomyopathy in mice. Circ. Res. *89*, 84–91.

45. Perng, M.D., Wen, S.F., van den IJssel, P., Prescott, A.R., and Quinlan, R.A. (2004). Desmin aggregate formation by R120G alphaB-crystallin is caused by altered filament interactions and is dependent upon network status in cells. Mol. Biol. Cell *15*, 2335–2346. https://doi.org/10.1091/mbc.e03-12-0893.

46. Sanbe, A., Osinska, H., Saffitz, J.E., Glabe, C.G., Kayed, R., Maloyan, A., and Robbins, J. (2004). Desmin-related cardiomyopathy in transgenic mice: a cardiac amyloidosis. Proc. Natl. Acad. Sci. USA *101*, 10132–10136. https://doi.org/10.1073/pnas.0401900101.

47. den Engelsman, J., Gerrits, D., de Jong, W.W., Robbins, J., Kato, K., and Boelens, W.C. (2005). Nuclear import of αB-crystallin is phosphorylation-dependent and hampered by hyperphosphorylation of the myopathy-related mutant R120G. J. Biol. Chem. *280*, 37139–37148.

48. Maloyan, A., Sanbe, A., Osinska, H., Westfall, M., Robinson, D., Imahashi, K.i., Murphy, E., and Robbins, J. (2005). Mitochondrial dysfunction and apoptosis underlie the pathogenic process in alpha-B-crystallin desmin-related cardiomyopathy. Circulation *112*, 3451–3461. https://doi.org/10.1161/CIRCULATIONAHA.105.572552.

49. Andley, U.P., Hamilton, P.D., Ravi, N., and Weihl, C.C. (2011). A knock-in mouse model for the R120G mutation of αB-crystallin recapitulates human hereditary myopathy and cataracts. PLoS One *6*, e17671.

50. Lilly, B., Galewsky, S., Firulli, A.B., Schulz, R.A., and Olson, E.N. (1994). D-MEF2: a MADS box transcription factor expressed in differentiating mesoderm and muscle cell lineages during Drosophila embryogenesis. Proc. Natl. Acad. Sci. USA *91*, 5662–5666. https://doi.org/10.1073/pnas.91.12.5662.

51. Bour, B.A., O'Brien, M.A., Lockwood, W.L., Goldstein, E.S., Bodmer, R., Taghert, P.H., Abmayr, S.M., and Nguyen, H.T. (1995). Drosophila MEF2, a transcription factor that is essential for myogenesis. Genes Dev. *9*, 730–741. https://doi.org/10.1101/gad.9.6.730.

52. Zhao, Z., Brooks, D., Guo, Y., and Geisbrecht, E.R. (2023). Identification of CryAB as a target of NUAK kinase activity in Drosophila muscle tissue. Genetics *225*, iyad167.

53. Guo, J., Huang, X., Dou, L., Yan, M., Shen, T., Tang, W., and Li, J. (2022). Aging and aging-related diseases: from molecular mechanisms to interventions and treatments. Signal Transduct. Target. Ther. *7*, 391. https://doi.org/10.1038/s41392-022-01251-0.

54. Graw, J. (2009). Genetics of crystallins: cataract and beyond. Exp. Eye Res. *88*, 173–189. https://doi.org/10.1016/j.exer.2008.10.011.

55. Sadeh, M., Rahat, D., Meiner, V., Fellig, Y., Arad, M., Schueler-Furman, O., Hu, Y., Li, Y., Bönnemann, C.G., and Lossos, A. (2021). Multi-system

neurological disorder associated with a CRYAB variant. Neurogenetics *22*, 117–125.

56. Hafizi, M., Chebotareva, N.A., Ghahramani, M., Moosavi-Movahedi, F., Khaleghinejad, S.H., Kurganov, B.I., Moosavi-Movahedi, A.A., and Yousefi, R. (2021). Structural and functional studies of D109A human αB-crystallin contributing to the development of cataract and cardiomyopathy diseases. PLoS One *16*, e0260306.
57. Li, Y., Li, S., and Wu, H. (2022). Ubiquitination-Proteasome System (UPS) and Autophagy Two Main Protein Degradation Machineries in Response to Cell Stress. Cells *11*, 851. https://doi.org/10.3390/cells11050851.
58. Kumar, A.V., Mills, J., and Lapierre, L.R. (2022). Selective autophagy receptor p62/SQSTM1, a pivotal player in stress and aging. Front. Cell Dev. Biol. *10*, 793328.
59. Ryan, S.M., Almassey, M., Burch, A.M., Ngo, G., Martin, J.M., Myers, D., Compton, D., Archie, S., Cross, M., Naeger, L., et al. (2021). Drosophila p38 MAPK interacts with BAG-3/starvin to regulate age-dependent protein homeostasis. Aging Cell *20*, e13481. https://doi.org/10.1111/acel.13481.
60. Arndt, V., Dick, N., Tawo, R., Dreiseidler, M., Wenzel, D., Hesse, M., Fürst, D.O., Saftig, P., Saint, R., Fleischmann, B.K., et al. (2010). Chaperone-assisted selective autophagy is essential for muscle maintenance. Curr. Biol. *20*, 143–148. https://doi.org/10.1016/j.cub.2009.11.022.
61. Brooks, D., Naeem, F., Stetsiv, M., Goetting, S.C., Bawa, S., Green, N., Clark, C., Bashirullah, A., and Geisbrecht, E.R. (2020). Drosophila NUAK functions with Starvin/BAG3 in autophagic protein turnover. PLoS Genet. *16*, e1008700. https://doi.org/10.1371/journal.pgen.1008700.
62. Clemen, C.S., Herrmann, H., Strelkov, S.V., and Schröder, R. (2013). Desminopathies: pathology and mechanisms. Acta Neuropathol. *125*, 47–75. https://doi.org/10.1007/s00401-012-1057-6.
63. Sharma, S., Conover, G.M., Elliott, J.L., Der Perng, M., Herrmann, H., and Quinlan, R.A. (2017). αB-crystallin is a sensor for assembly intermediates and for the subunit topology of desmin intermediate filaments. Cell Stress Chaperones *22*, 613–626. https://doi.org/10.1007/s12192-017-0788-7.
64. Houck, S.A., Landsbury, A., Clark, J.I., and Quinlan, R.A. (2011). Multiple sites in αB-crystallin modulate its interactions with desmin filaments assembled in vitro. PLoS One *6*, e25859. https://doi.org/10.1371/journal.pone.0025859.
65. Kedia, N., Arhzaouy, K., Pittman, S.K., Sun, Y., Batchelor, M., Weihl, C.C., and Bieschke, J. (2019). Desmin forms toxic, seeding-competent amyloid aggregates that persist in muscle fibers. Proc. Natl. Acad. Sci. USA *116*, 16835–16840. https://doi.org/10.1073/pnas.1908263116.
66. Pilotto, A., Marziliano, N., Pasotti, M., Grasso, M., Costante, A.M., and Arbustini, E. (2006). alphaB-crystallin mutation in dilated cardiomyopathies: low prevalence in a consecutive series of 200 unrelated probands. Biochem. Biophys. Res. Commun. *346*, 1115–1117.
67. Cannone, E., Guglielmi, V., Marchetto, G., Tobia, C., Gnutti, B., Cisterna, B., Tonin, P., Barbon, A., Vattemi, G., and Schiavone, M. (2023). Human Mutated MYOT and CRYAB Genes Cause a Myopathic Phenotype in Zebrafish. Int. J. Mol. Sci. *24*, 11483.
68. Batonnet-Pichon, S., Behin, A., Cabet, E., Delort, F., Vicart, P., and Lilienbaum, A. (2017). Myofibrillar Myopathies: New Perspectives from Animal Models to Potential Therapeutic Approaches. J. Neuromuscul. Dis. *4*, 1–15. https://doi.org/10.3233/JND-160203.
69. Xu, M., Ji, J., Jin, D., Wu, Y., Wu, T., Lin, R., Zhu, S., Jiang, F., Ji, Y., Bao, B., et al. (2023). The biogenesis and secretion of exosomes and multivesicular bodies (MVBs): Intercellular shuttles and implications in human diseases. Genes Dis. *10*, 1894–1907. https://doi.org/10.1016/j.gendis.2022.03.021.
70. Babst, M. (2011). MVB vesicle formation: ESCRT-dependent, ESCRT-independent and everything in between. Curr. Opin. Cell Biol. *23*, 452–457.
71. van Niel, G., D'Angelo, G., and Raposo, G. (2018). Shedding light on the cell biology of extracellular vesicles. Nat. Rev. Mol. Cell Biol. *19*, 213–228. https://doi.org/10.1038/nrm.2017.125.
72. Linnemannstöns, K., Karuna M, P., Witte, L., Choezom, D., Honemann-Capito, M., Lagurin, A.S., Schmidt, C.V., Shrikhande, S., Steinmetz, L.K., Wiebke, M., et al. (2022). Microscopic and biochemical monitoring of endosomal trafficking and extracellular vesicle secretion in an endogenous in vivo model. J. Extracell. Vesicles *11*, e12263. https://doi.org/10.1002/jev2.12263.
73. Sacconi, S., Féasson, L., Antoine, J.C., Pécheux, C., Bernard, R., Cobo, A.M., Casarin, A., Salviati, L., Desnuelle, C., and Urtizberea, A. (2012). A novel CRYAB mutation resulting in multisystemic disease. Neuromuscul. Disord. *22*, 66–72.
74. Kim, H.S., Lee, Y., Lim, Y.A., Kang, H.J., and Kim, L.S. (2011). αB-Crystallin is a Novel Oncoprotein Associated with Poor Prognosis in Breast Cancer. J. Breast Cancer *14*, 14–19. https://doi.org/10.4048/jbc.2011.14.1.14.
75. Zhao, Z., Brooks, D., Guo, Y., and Geisbrecht, E.R. (2023). Identification of CryAB as a target of NUAK kinase activity in Drosophila muscle tissue. Genetics *225*, iyad167. https://doi.org/10.1093/genetics/iyad167.
76. Kore, R.A., and Abraham, E.C. (2016). Phosphorylation negatively regulates exosome mediated secretion of cryAB in glioma cells. Biochim. Biophys. Acta *1863*, 368–377.
77. Xu, Z., Paparcone, R., and Buehler, M.J. (2010). Alzheimer's abeta(1-40) amyloid fibrils feature size-dependent mechanical properties. Biophys. J. *98*, 2053–2062. https://doi.org/10.1016/j.bpj.2009.12.4317.
78. Liang, R., Khursheed, A., Tahirbegi, B., Torres-Flores, A.P., Qi, S., Tian, Y., Zhang, H., Szwedziak, P., Volkov, V.A., Darbari, V.C., and Viles, J.H. (2025). Amyloid-β oligomers, curvilinear and annular assemblies, imaged by cryo-ET, cryo-EM, and AFM. Sci. Adv. *11*, eadx9030. https://doi.org/10.1126/sciadv.adx9030.
79. Jansen, R., Grudzielanek, S., Dzwolak, W., and Winter, R. (2004). High pressure promotes circularly shaped insulin amyloid. J. Mol. Biol. *338*, 203–206. https://doi.org/10.1016/j.jmb.2004.02.056.
80. Béhin, A., Salort-Campana, E., Wahbi, K., Richard, P., Carlier, R.-Y., Carlier, P., Laforêt, P., Stojkovic, T., Maisonobe, T., Verschueren, A., et al. (2015). Myofibrillar myopathies: state of the art, present and future challenges. Rev. Neurol. *171*, 715–729.
81. Moro, E., Vettori, A., Porazzi, P., Schiavone, M., Rampazzo, E., Casari, A., Ek, O., Facchinello, N., Astone, M., Zancan, I., et al. (2013). Generation and application of signaling pathway reporter lines in zebrafish. Mol. Genet. Genomics. *288*, 231–242. https://doi.org/10.1007/s00438-013-0750-z.
82. Kimmel, C.B., Ballard, W.W., Kimmel, S.R., Ullmann, B., and Schilling, T.F. (1995). Stages of embryonic development of the zebrafish. Dev. Dyn. *203*, 253–310. https://doi.org/10.1002/aja.1002030302.
83. Guglielmi, V., Pancheri, E., Cannone, E., Nigro, V., Malatesta, M., Vettori, A., Giorgetti, A., Torella, A., Aurino, S., Cisterna, B., et al. (2023). A novel in-frame deletion in MYOT causes an early adult onset distal myopathy. Clin. Genet. *104*, 705–710. https://doi.org/10.1111/cge.14413.
84. Arndt, V., Dick, N., Tawo, R., Dreiseidler, M., Wenzel, D., Hesse, M., Fürst, D.O., Saftig, P., Saint, R., Fleischmann, B.K., et al. (2010). Chaperone-assisted selective autophagy is essential for muscle maintenance. Curr. Biol. *20*, 143–148.
85. Rai, M., Curley, M., Coleman, Z., Nityanandam, A., Jiao, J., Graca, F.A., Hunt, L.C., and Demontis, F. (2021). Analysis of proteostasis during aging with western blot of detergent-soluble and insoluble protein fractions. STAR Protoc. *2*, 100628. https://doi.org/10.1016/j.xpro.2021.100628.
86. Schultz, S.W., Nilsson, K.P.R., and Westermark, G.T. (2011). Drosophila melanogaster as a model system for studies of islet amyloid polypeptide aggregation. PLoS One *6*, e20221. https://doi.org/10.1371/journal.pone.0020221.
87. Menter, T., Bachmann, M., Grieshaber, S., and Tzankov, A. (2017). A More Accurate Approach to Amyloid Detection and Subtyping: Combining in situ Congo Red Staining and Immunohistochemistry. Pathobiology *84*, 49–55. https://doi.org/10.1159/000447304.

STAR★METHODS

KEY RESOURCES TABLE

REAGENT or RESOURCE	SOURCE	IDENTIFIER
Antibodies		
Polyclonal rabbit anti-CryAB (1:200 for tissue; 1:1000 for Western blot)	BosterBio	Cat# DZ33926
Polyclonal mouse anti-Ubi UBCJ2 (1:200 for tissue; 1:1000 for Western blot)	Enzo	Cat# ABS840 RRID:AB_2935893
Polyclonal rabbit anti-p62 (1:200 for tissue; 1:1000 for Western blot)	Helmut Kramer	N/A
Polyclonal rabbit anti-Ref(2)p/p62 (1:200 for tissue)	Abcam	Cat# ab178440 RRID:AB_2938801
Polyclonal rabbit anti-Stv (1:200 for tissue)	PMID: 23986815	N/A
Mouse monoclonal anti-ATP5α (1:20,000 for Western blot)	Abcam	Cat# ab14748; RRID:AB_301447
Mouse monoclonal anti-hDesmin (1:200 for tissue)	Invitrogen	Cat# MA5-13259; RRID:AB_11000611
Mouse monoclonal anti-GFP (1:25 for tissue)	DSHB	Cat# 12E6; RRID:AB_3696611
Mouse monoclonal anti-HA 6E2 (1:25 for tissue)	Cell Signaling	Cat# 2367; RRID:AB_10691311
Mouse monoclonal anti-SNCA (1:200 for tissue)	Santa Cruz Biotechnology	Cat# sc-12767; RRID:AB_628318
Mouse monoclonal anti-Rab7 (1:200 for tissue)	DSHB	Cat# Rab7, RRID:AB_2722471
Rabbit polyclonal anti-Rab5 (1:200 for tissue)	Abcam	Cat# ab31261; RRID:AB_882240
Goat anti-mouse Alexa Fluor 488 (1:400 for tissue)	Invitrogen	Cat#A11001; RRID:AB_2534069
Goat anti-mouse Alexa Fluor 594 (1:400 for tissue)	Invitrogen	Cat#A11005; RRID:AB_2534073
Goat anti-rabbit Alexa Fluor 488 (1:400 for tissue)	Invitrogen	Cat# A11034; RRID:AB_2576217
Donkey anti-rabbit Alexa Fluor 594 (1:400 for tissue)	Invitrogen	Cat# A21207; RRID:AB_141637
IRDye 680RD Goat anti-mouse IgG secondary antibody (1:10000)	LI-COR	Cat# 926-68070; RRID:AB_10956588
IRDye 800CW Goat anti-Mouse IgG secondary antibody (1:10000)	LI-COR	Cat# 926-32210; RRID:AB_621842
Chemicals, peptides, and recombinant proteins		
Halt protease inhibitor cocktail	Thermo Scientific	Cat#1861278
Halt phosphatase inhibitor cocktail	Thermo Scientific	Cat# 1862495
Congo Red	Sigma-Aldrich	Cat# C6767
ThioflavinT	MedChemExpress	Cat# HY-D0218
Hoechst (1:400)	Invitrogen	Cat# H3569
Critical commercial assays		
Revert 700 Total Protein Stain	LI-COR	Cat# NC1572646
Qiagen Maxi Kit	Qiagen	Cat# 12163
20S Proteosome activity kit	Cayman Chemical	Cat# 10008041
Deposited data		
Raw/processed MS data	MassIVE	MSV000100788
Raw/processed MS data	ProteomeXchange	PXD074306
Experimental models: Organisms/strains		
UAS-mCherry RNAi	Bloomington *Drosophila* Stock Center (BDSC)	BL35785 RRID:BDSC_35785
Cyo,Tb balancer	BDSC	BL36335; RRID:BDSC_36335;
pUAST_attB-CryAB WT	PMID: 37713608	Progenitor: RRID:BDSC_9736; PBac{y+-attP-9A}VK00018

(*Continued on next page*)

Continued

REAGENT or RESOURCE	SOURCE	IDENTIFIER
pUAST_attB-CryAB S68A	PMID: 37713608	Progenitor: RRID:BDSC_9736; PBac{y+-attP-9A}VK00018
pUAST_attB-CryAB S68E	PMID: 37713608	Progenitor: RRID:BDSC_9736; PBac{y+-attP-9A}VK00018
pUAST_attB-CryAB S70A	PMID: 37713608	Progenitor: RRID:BDSC_9736; PBac{y+-attP-9A}VK00018
pUAST_attB-CryAB S70E	PMID: 37713608	Progenitor: RRID:BDSC_9736; PBac{y+-attP-9A}VK00018
pUAST_attB-CryAB S68/70A	PMID: 37713608	Progenitor: RRID:BDSC_9736; PBac{y+-attP-9A}VK00018
pUAST_CryAB D109A	This paper	Progenitor: RRID:BDSC_9736; PBac{y+-attP-9A}VK00018
pUAST_CryAB D109H	This paper	Progenitor: RRID:BDSC_9736; PBac{y+-attP-9A}VK00018
pUAST_CryAB R120G	This paper	Progenitor: RRID:BDSC_9736; PBac{y+-attP-9A}VK00018
pUAST_CryAB R157H	This paper	Progenitor: RRID:BDSC_9736; PBac{y+-attP-9A}VK00018
pUAST_hDesmin (aa117-349)	This paper	Progenitor: w[1118]
UAS-mCherry-Tsp96F	PMID: 36103151	https://doi.org/10.1002/jev2.12263
UAS-Tsp96F RNAi	BDSC	BL40901; RRID:BDSC_40901
UAS-Rab27-YFP	BDSC	BL9810 RRID:BDSC_9810
UAS-Rab27 RNAi	BDSC	BL31887 RRID:BDSC_31887
UAS-Alix-Flag-HA	BDSC	BL95213 RRID:BDSC_95213
UAS-hTSG101-HA	BDSC	BL77977 RRID:BDSC_77977
UAS-SNCA	BDSC	BL51376 RRID:BDSC_51376
UAS-hCD63-GFP	Dr.Young Kwon	UAS-hCD63-GFP
Recombinant DNA		
pUAST vector	*Drosophila* Genomics Resource Center (DGRC)	RRID:DGRC_1000
pUAST_attB vector	(DGRC)	RRID:DGRC_1419
Plasmid: pUAST_attB-CryAB WT	PMID: 37713608	Flybase:FBal0397187
Plasmid: pUAST_attB-CryAB S68A	PMID: 37713608	Flybase:FBal0397188
Plasmid: pUAST_attB-CryAB S68E	PMID: 37713608	Flybase: FBal0397189
Plasmid: pUAST_attB-CryAB S70A	PMID: 37713608	Flybase: FBal0397190
Plasmid: pUAST_attB-CryAB S70E	PMID: 37713608	Flybase: FBal0397191
Plasmid: pUAST_attB-CryAB S68/70A	PMID: 37713608	Flybase: FBal0397192
Plasmid: pUAST_attB-CryAB D109A	This paper	Progenitors: Genscript site-directed mutagenesis; pUASTattB vector
Plasmid: pUAST_attB-CryAB D109H	This paper	Progenitors: Genscript site-directed mutagenesis; pUASTattB vector
Plasmid: pUAST_attB-CryAB R120G	This paper	Progenitors: Genscript site-directed mutagenesis; pUASTattB vector
Plasmid: pUAST_attB-CryAB R157H	This paper	Progenitors: Genscript site-directed mutagenesis; pUASTattB vector

(*Continued on next page*)

Continued

REAGENT or RESOURCE	SOURCE	IDENTIFIER
Plasmid: pUAST_hDesmin (aa117-349)	This paper	Progenitors:Genscript gene synthesis; pUAST vector
Software and algorithms		
Empiria Studio Software	LI-COR Biosciences	RRID:SCR_022512
Image J	https://imagej.net/ij/	RRID:SCR_003070
Graphpad Prism	https://www.graphpad.com/	RRID:SCR_002798
Biorender	https://www.biorender.com/	RRID:SCR_018361

EXPERIMENTAL MODEL AND STUDY PARTICIPANT DETAILS

Drosophila stocks and husbandry

Drosophila melanogaster was used for all *Drosophila* experiments. Males and females were used for larval muscle experiments and only females were used for adult muscle experiments to control for sex differences. Only staged L3 larva were used for larval muscle experiments. For aging experiments, only day 2 or day 10 flies were used for adult experiments. Fly stocks were maintained on Bloomington *Drosophila* Stock Center (BDSC) Cornmeal Food (https://bdsc.indiana.edu/information/recipes/bloomfood.html). All *Drosophila* genotypes are described here. *Drosophila* stocks obtained from the BDSC are indicated with BL followed by the stock number. *Mef2*-Gal4 (BL27390) was used to direct expression in larval muscles and the IFMs. UAS-*mCherry RNAi* (BL35785) was used as a control for Gal4-mediated experiments. BDSC stocks used for the analysis of EV markers: UAS-*TSG101-HA* (BL77977), UAS-*Alix-Flag-HA* (BL95213), and UAS-*YFP-Rab27* (BL9810). UAS-*SCNA* served as a negative control (BL51376). RNAi lines from BDSC: UAS-*Tsp6F RNAi* (BL40901). The UAS-*mCh-Tsp96F* flies were a gift from Dr. Julia Groß[72] and the UAS-*hCD63-GFP* flies were obtained from Dr. Young Kwon.

Zebrafish maintenance

AB Zebrafish wildtype and the previously generated transgenic reported line *tg(Kdrl:EGFP)* were kindly provided by the Zebrafish Facility of the University of Padova.[81] Zebrafish manipulation and experiments have been performed according to the formal Italian Ministry of Health Authorization n. 60/2023 and followed all standard Animal Care Standard Operating Procedures (ARRIVE guidelines 2.0). All lines have been maintained at 28.5°C, with a 14-10 light-dark cycle in aerated saline water, in the Zebrafish Facility at the University of Brescia according to standard protocols.[82] To allow animal breeding, egg deposition and fertilization, male and female animals were separated in the late afternoon and free to start courtship the next morning to allow mating events. Embryos were then injected at 1 cell stage with 25 ng/uL of each plasmid (hCRYAB WT, hCRYAB G154S, hMYOT WT and hMYOT S95I) as previously described.[67,83] Embryos were collected and maintained at 28.5°C in embryo medium (0.19 g/L CaSO4, 0.1 g/L Instant Ocean Salt e 0.1 g/L NaHCO3). All manipulation and experiments were performed within 120 h post-fertilization (hpf) and thus did not require formal authorization according to Standard Operating Procedures of the Animal Care, the Use Committee of the University of Brescia and Italian Ministry of Health directives.

Human muscle biopsy collection

The study was conducted in accordance with the Declaration of Helsinki, and approved by the Ethics Committee of Azienda Ospedaliera Universitaria Integrata di Verona (BIOB-NEU-DNA-2014, prog. 430CESC). All deidentified patients underwent open muscle biopsy at the Neuromuscular Center of Clinical Neurology, Department of Neurosciences, Biomedicine and Movement Sciences, University of Verona, Verona, Italy. Muscle biopsies were performed for diagnostic purpose after written informed consent.

METHOD DETAILS

Creation of transgenic flies

CryAB

UAS-CryAB (wild-type) and UAS-mediated phosphosite mutations (*S68A*, *S68E, S70, S70E, S68/70A*) were previously published.[52] To generate UAS-human CryAB mutations (*D109A, D109H, R120G* or *R157H*), cDNA corresponding to the coding region of wild-type *CryAB-RC* was synthesized by Genscript, subcloned into the pUAST_attB vector using EcoRI/XbaI sites, and subjected to site-directed mutagenesis. Plasmid DNA was verified by sequencing and purified using the Qiagen Maxi kit (Hilden, Germany). Constructs were sent to Rainbow Transgenic Flies, Inc. (Camarillo, CA) for injection into line # 9736 for integration at the PhiC31landing site (53B2). All resulting transgenic lines were balanced over the w; ScO/Cyo,Tb balancer (BL36335). Each CryAB line was then recombined with the *Mef*-Gal4 driver and maintained at 18°C.

hDesmin

cDNA corresponding to the amyloidogenic region of human *Desmin* (aa 117-348)[65] was synthesized by Genscript and subcloned into the pUAST vector using EcoRI/XbaI sites. Plasmid DNA was verified by sequencing, purified using the Qiagen Maxi kit (Hilden, Germany), and Rainbow Transgenic Flies, Inc. (Camarillo, CA) for injection into *y+* embryos. The resulting *w+* fly lines were balanced over the w; ScO/Cyo,Tb (BL36335) or w; TM3,Sb/TM6b,Tb (Geisbrecht lab) balancers. Experiments in this paper used an insertion on chromosome 2.

Visualization of muscle tissue

Larval muscle staining

Wandering L3 larvae were placed onto a Sylgard plate, pinned near the mouth hooks at the anterior end, and the internal organs were removed. Muscle carcasses were fixed in 4% formaldehyde, rinsed 3x in phosphate buffered saline + 0.5% Tween (PBT) and blocked for 30 min in 5% normal goat serum (NGS). Primary antibodies were incubated overnight at 4 °C in PBT, washed 3x in PBT followed by secondary antibody incubation for 2hrs at room temperature. Samples were then washed 3x in PBT and mounted in glycerol + 0.5% n-propyl gallate (anti-fade reagent with 10% 20mM Tris buffer, pH=8.0). Tissues were stained with rabbit anti-CryAB (1:200, #DZ33926, Boster Bio, Pleasanton, California) followed by Alexa Fluor anti-rabbit 488 (1:400; A11001, Invitrogen, Waltham, MA) and phalloidin 594 to label F-actin (1:400, A12381 Molecular Probes, Invitrogen, Waltham, MA).

Adult IFM staining

Day 2 or Day 10 female adult flies were anaesthetized on a CO_2 plate and the head, wings and abdomen were removed. The remaining whole thoraces were fixed in 4% methanol-free formaldehyde (Polysciences, Warrington, PA) for 30 minutes at room temperature and washed three times in PBT before bissection using a sharp blade. Immunostaining was performed as described above using the following primary antibodies: rabbit anti-CryAB (1:200, #DZ33926, Boster Bio, Pleasanton, California), mouse anti-Ubi UBCJ2 (1:200, ENZ-ABS840, Enzo Life Sciences, Farmingdale, NY); rabbit anti-p62 (1:200, ab178440, Abcam, Cambridge, MA), rabbit anti-Stv (1:200),[84] rabbit anti-hDesmin (1:200, AB_11000611, Invitrogen, Waltham, MA), mouse anti-HA 6E2 (1:400, #2367, Cell Signaling, Danvers, MA), anti-Rab7 (1:200, AB-2722471, DSHB, Iowa, IA), anti-Rab5 (1:200, ab31261, Abcam, Cambridge, United Kingdom), and anti-SNCA (1:200, sc-12767, Santa Cruz Biotechnology, Dallas, TX). Secondary antibodies were either Alexa Fluor anti-rabbit 488 (1:400, A11034, Invitrogen, Waltham, MA), Alexa Fluor anti-rabbit 594 (1:400, A21207, Invitrogen, Waltham, MA), Alexa Fluor anti-mouse 488 (1:400, A11001, Invitrogen, Waltham, MA), Alexa Fluor anti-mouse 594 (1:400, A-11005, Invitrogen, Waltham, MA). Alexa Fluor Phalloidin 647 were used to label F-actin (1:400, A22287, Invitrogen, Waltham, MA).

Adult heart tube staining

Day 2 female adult flies were anaesthetized on a CO_2 plate. Whole flies were fixed in 4% formaldehyde overnight at room temperature, dissected to reveal the heart tube, and immunostained as described above with rabbit anti-CryAB (1:200, #DZ33926, Boster Bio, Pleasanton, California) and mouse anti-Ubi UBCJ2 (1:200, ENZ-ABS840, Enzo Life Sciences, Farmingdale, NY). Alexa Fluor anti-rabbit 488 (1:400, A11034, Invitrogen, Waltham, MA), Alexa Fluor rabbit 594 (1:400, A21207, Invitrogen, Waltham, MA), Alexa Fluor anti-mouse 488 (1:400, A11001, Invitrogen, Waltham, MA), Alexa Fluor mouse 594 (1:400, A-11005, Invitrogen, Waltham, MA). Phalloidin 647 were used to label F-actin (1:400, A22287, Invitrogen, Waltham, MA).

Zeiss image processing

Images were captured using a Zeiss 700 confocal microscope. Image processing and analysis were performed using a combination of Zen Black (Zeiss), ImageJ (NIH), and Adobe Photoshop. All fly muscle images taken at 63x are displayed as a single plane confocal images.

3D morphological analysis of fly muscles

Z-stack images were opened with Imaris (version 10.2, Oxford Instruments). Four fluorescence channels of cellular structures in each Z-stack image were assigned different colors using the 'Display Adjustment' tool. The intensity and contrast of each channel were adjusted individually. The 'Volume' tool was used to generate a 3D volume view of each channel. In the 'Volume Settings' stub, the 'Normal Shading' mode was chosen to display the volume view and 'Opacity' was set to 0.39. The 'Min' and 'Max' parameters were adjusted to ensure that the fluorescence signal channel in each channel was accurately represented within the corresponding volume rendering. 3D animations of cellular structures were created using the horizontal and vertical rotation functions, and 3D images were captured with the 'Snapshot' tool.

Western blotting to assess soluble and insoluble fractions

Day 2 or Day 10 adult female flies were anaesthetized on a CO_2 plate and the head, wings and abdomen were removed and prepared as described with minor modifications.[85] Three thoraces for each genotype were homogenized in 50 µl of freshly prepared TritonX-100 cell lysis buffer: 1% TritonX-100 cell in PBS, 1x Halt Phosphatase inhibitor cocktail (#1862495, Thermo Scientific, Waltham, MA), 1x Halt Protease inhibitor cocktail (#1861278, Thermo Scientific, Waltham, MA) on ice with the aid of a tissue homogenizer (Kimble). Homogenates were then centrifuged at 21,000 x g at 4°C for 10 min and the supernatant (soluble fraction) was collected in 3x SDS sample buffer: 188 mM Tris-HCl (pH 6.8), 3% (w/v) SDS, 30% (v/v) glycerol, 0.01% (w/v) bromophenol-blue, and 15% (v/v) β-mercaptoethanol, and boiled at 95°C for 5 min before gel loading. The remaining pellet (insoluble fraction) was washed with Triton X-100 buffer 3x and the samples were centrifuged at 21,000 x g for 5 mins at 4°C. The supernatant was discarded and the pellet was resuspended with 50uL freshly prepared Urea/SDS buffer (Urea and SDS solubilization buffer 10mL: 8M Urea, 2.5mL 20% SDS, 1mL

10X RIPA buffer, 1x Halt Phosphatase inhibitor cocktail, and 1x Halt Protease inhibitor cocktail with homogenization. The sample was centrifuged at 21,000 x g at 4°C for 10 mins and the resulting insoluble supernatant was transferred to a new tube. 50uL 3x SDS sample buffer was added and the sample was boiled at 95°C for 5 min before gel loading. The soluble or insoluble protein samples were separated by sodium dodecyl sulfate polyacrylamide gel electrophoresis (SDS-PAGE) and transferred to the nitrocellulose blotting membrane (pore size 0.45 μm, Cytiva, Marlborough, MA) using the Trans-Blot® TurboTM Transfer System (Bio-Rad, Hercules, CA). Membranes were probed with rabbit anti-CryAB (1:1000, #DZ33926, Boster Bio, Pleasanton, CA), or rabbit anti-Ref(2)p/p62 (ab178440, 1:2000, Abcam, Cambridge, UK). IRDye 800CW secondary antibodies (LI-COR Biosciences, Lincoln, NE) were used at 1:10000 and Revert 700 Total Protein Stain (LI-COR Biosciences, Lincoln, NE) or anti-ATP5α (1:20000, ab14748, Abcam, Cambridge, United Kingdom) was used as a loading control. Membranes were developed using the LI-COR Odyssey XF and quantitation of relative protein levels was performed in Empiria Studio Software (LI-COR Biosciences, Lincoln, NE). N=3 for all Western blots.

Lethal stage analysis

Adult survival

Lifespan measurements for adult flies was performed at 31°C in an incubator with 60% humidity. For each of the analyzed genotypes, virgin female flies were collected at Day 1 and transferred to fresh media each day. The number of dead flies was recorded at 24 hr intervals until the end of lifespan. N≥3 biological replicates with each replicate consisting of at least 50 flies.

Pupal lethality

To measure the stage of pupal lethality for each genotype, the F1 generation was shifted to the 31°C incubator at the embryo stage. After the flies eclosed as adults, the remaining empty pupa cases or dead pupa in each vial were recorded. N≥3 biological replicates with each replicate consisting of at least 80 pupae.

Quantification of CryAB aggregates or inclusions

For each muscle thorax, 10 randomly selected confocal images were selected for quantification. Ubi was used as a marker for aggregates in double labeling experiments with CryAB. Either CryAB alone or CryAB and hDesmin or HA (for Alix and TSG101) were used to label inclusions. For quantification, the number of Ubi(+)/CryAB(+) aggregates or CryAB(+) and/or hDesmin(+) structures were manually counted and divided by the total area of muscles per picture to calculate the average number/2500 μm^2 (50 x 50 μm) in each image. Measurements of CryAB inclusion body area was analyzed using the Wand tool of Image J. This experimental approach was applied consistently throughout the study to analyze individual CryAB mutant expression, as well as in co-expression models including CryAB mutant/Desmin, CryAB mutant/mCherry RNAi, CryAB mutant/Alix-HA, CryAB mutant/mCherry-Tsp96F, and CryAB mutant/Tsp96F RNAi. N≥10 for each genotype. See also quantification and statistical analysis section.

Transmission Electron Microscopy (TEM)

Adult female flies were reared at 31°C until Day 10, anaesthetized on a CO_2 plate and the head, wings and abdomen were removed. Each fly thorax was dissected in 0.1 M cacodylate buffer and fixed in 1% glutaraldehyde/4% paraformaldehyde in 0.1 M cacodylate buffer overnight at 4°C followed by three washes with 0.1 M cacodylate buffer. The samples were treated with 1% OsO4 for 1 h at 4 °C. After washing with ddH2O, the samples were dehydrated in a gradient series using 30%, 50%, 70%, 95%, and 100% ethanol solutions at room temperature. The samples were then infiltrated using series epoxy resin at room temperature and mounted in pure resin. After polymerization at 60°C for 2 Days, 90 nm semi-thin sections were cut and stained with toluidine blue stain to determine orientation. Ultrathin sections were stained with uranyl acetate and lead citrate for observation under a JEOL JEM 1400 electron microscope at the University of Kansas Medical School.

CryAB inclusion extraction from muscle

Adult *Drosophila* were anesthetized on a CO_2 pad, and thoraces were carefully dissected and transferred into 50 μL of phosphate-buffered saline (PBS) containing protease and phosphatase inhibitors, along with 1-phenyl 2-thiourea (PTU) to prevent melanization. Samples were processed on ice to preserve protein integrity. Thoracic tissue was homogenized thoroughly and centrifuged at 1,000 × g for 3–5 minutes at 4°C. The resulting supernatant was collected and applied to L-lysine-coated slides to allow inclusions to settle for 5 minutes at 4°C. Samples were then fixed with 1 mL of 4% formaldehyde in PBS for 30 minutes in the dark. After fixation, the slides were rinsed twice with PBS containing 0.3% Triton X-100 (PBT). Antibody staining was performed as described above.

Congo red and CryAB staining

Slides with isolated inclusions from either muscle or hemolymph were incubated in Solution A (NaCl-saturated 80% ethanol with 0.01% NaOH) for 20 mins. This was followed by a 20 min incubation in Solution B (2.5 g Congo red and 1 g potassium hydroxide dissolved in 500 mL of 80% ethanol) at room temperature. Samples were then sequentially rinsed in absolute ethanol and xylene before immunofluorescence staining.[86,87] Following Congo red staining, slides were washed 2–3 times with PBT. To prevent disruption of Congo red signals during antibody staining, blocking was performed using PBS supplemented with 5% normal goat serum (NGS) for 30 minutes (PBT was avoided at this step). Primary antibodies were diluted in the same PBS blocking buffer and incubated with samples overnight at 4°C. The following day, slides were washed twice in PBT for 5 minutes each. Samples were re-blocked in PBS + 5% NGS for 30 minutes before incubation with fluorescently labeled secondary antibodies Alexa Fluor

anti rabbit 488 (1:400, A11034, Invitrogen, Waltham, MA) for 2hrs at room temperature. Finally, slides were washed twice in PBT and mounted for imaging.

Thioflavin T (ThT) assay

Thioflavin T assays were performed using inclusions extracted from adult muscle thoraces as shown in Figure 5A. The final inclusion pellet was resuspended in 200 μL PBS. A 1 mM ThT stock solution was prepared in ddH_2O and diluted in PBS to a working concentration of 25 μM (25 μL of 1 mM ThT added to 975 μL PBS; sample volumes were adjusted accordingly). Inclusion samples (10 μL, 25 μL, 50 μL, or 100 μL) were added to wells of a 96-well plate containing the ThT working solution. Plates were covered to protect from light and incubated in a shaking incubator at 37 °C for 1 hr. Fluorescence was measured using a Biotek Synergy H1 microplate reader with excitation at 450 nm and emission at 485 nm.

Hemolymph inclusion extraction

Adult *Drosophila* were anesthetized on a CO_2 pad, and thoraces were dissected and transferred into 500 μL microcentrifuge tubes containing 50 μL of phosphate-buffered saline (PBS) supplemented with protease and phosphatase inhibitors, and 1-phenyl 2-thiourea (PTU). A small hole was pierced at the bottom of a 500 μL tube, which was then placed inside a 1 mL collection tube to allow hemolymph to drain during centrifugation. Hemolymph was collected by centrifugation at 21,130 × g for 5 minutes at 4°C. The supernatant was then sequentially centrifuged at 700 × g for 20 minutes, 1,500 × g for 10 minutes, and 14,000 × g for 20 minutes to purify EVs from the hemolymph.[72] The final EV pellet (14000 x g pellet) was resuspended in 200 μL of PBS. This EV preparation was subsequently used for Congo Red staining, CryAB immunostaining, and mass spectrometry.

Mass spectrometry

300 adult thoraces of each genotype were used for the inclusion hemolymph extraction of mass spectrometry. Inclusions in EV samples were dried in a SpeedVac concentrator until reduced to ~100 μL. Samples were lysed by adding an equal volume of RIPA buffer supplemented with protease inhibitors, phosphatase inhibitors, and nuclease, followed by incubation on ice for 30 minutes. Lysates were then sonicated in a water bath for 15 minutes. For reduction of disulfide bonds, 20 μL of 50 mM TCEP was added (final concentration 5 mM), and samples were incubated at 55°C for 30 minutes. Cysteine alkylation was performed by adding 6 μL of 375 mM iodoacetamide (IAA; final concentration 10 mM) and incubating the mixture at room temperature in the dark for 30 minutes. Proteins were precipitated by adding 900 μL of acetone (1:5 dilution) and incubating overnight at −20 °C. The following day, samples were centrifuged at 14,000 × g for 10 minutes at 4°C. Supernatants were removed, and protein pellets were air-dried for 15 minutes at room temperature. Pellets were then resuspended in 100 μL of 50 mM triethylammonium bicarbonate (TEAB) containing 2 mM $CaCl_2$. Proteins were digested overnight at 37°C with 500 ng of trypsin (0.1 mg/mL) at 500 rpm. Digestion was quenched by adding 10% formic acid to a final concentration of 1%.

LC–MS/MS analysis

Peptide concentrations were determined using a NanoDrop UV spectrophotometer. Based on these measurements, 0.5 μL of each sample was loaded onto a C18 reversed-phase column and analyzed using an Orbitrap Ascend mass spectrometer equipped with FAIMS for LC–MS/MS acquisition at the University of Kansas Medical School.

Mass spectrometry data processing

Raw mass spectrometry data were processed using Proteome Discoverer with the SeQuest search engine, using the Drosophila melanogaster UniProt protein database (downloaded July 18, 2025). The "Proteins" output table includes all proteins detected across samples. Grouped abundance values represent the median protein abundance across sample replicates (columns Z–AC). Normalized and raw abundance values are provided in columns AH–AS and AT–BE, respectively. For each pairwise comparison, an abundance ratio (AR) and $\log_2$(AR) were calculated. Proteins with $\log_2(AR) \geq 1$ were considered significantly enriched in the numerator sample, while proteins with $\log_2(AR) \leq -1$ were considered significantly depleted. These proteins are marked in green (≥ 1) or red (≤ -1) in columns I. Statistical significance was assessed using p-values, with proteins meeting $p \leq 0.05$ highlighted in yellow in columns J. GraphPad Prism was used to generate volcano plots. Gene Ontology (GO) biological process enrichment analyses were performed using the PANTHER–based Pangea GO analysis platform. N=3.

Proteasome activity assay

Drosophila 20S proteasome activity was determined using the 20S Proteasome Assay Kit (#10008041, Cayman Chemical, Ann Arbor, MI). Crosses were reared at 25°C and transferred to 31°C after eclosion. For each genotype, 5 adult female flies at either Day 2 or Day 10 were dissected to remove the head, wings, and abdomen. The thorax was transferred to a 1.5 ml microcentrifuge tube containing 200 μl of ice-cold 20S Proteasome Lysis Buffer. After homogenization on ice, the tube was centrifuged at 12000 x g for 5 minutes at 4°C, and the supernatant was transferred to a new tube and kept on ice. 5 wells were used for each genotype in a 96-well plate. 10 μl of 20S Proteasome Assay Buffer was added to each well with increasing amounts of supernatant (0, 5, 10, 20, and 50 μl in wells 1-5, respectively). 20S Proteasome Lysis Buffer was added to each well to bring the total volume up to 100 μl. For samples treated with the 20S Proteasome Inhibitor (EGCG), 10 μl of inhibitor was added instead of Assay buffer. Finally, 10 μl of the 20S Proteasome Substrate (SUC-LLVY-AMC) was added to each well. The plate was incubated at 37°C for 1 hr. After 1 hr the fluorescence intensity for each well was read using a Biotek Synergy HI plate reader (excitation = 360 nm, emission 480 nm).

Yeast two-hybrid (Y2H)

Y2H assays were carried out by Hybrigenics Services as previously described.[61] To summarize,the coding sequence of the full-length *D. melanogaster* NUAK/CG43143 (GenBank accession number NM_206469.3) was PCR-amplified and cloned in frame with the Gal4 DNA binding domain (DBD) into plasmid pB66 as a C-terminal fusion to Gal4 (Gal4-bait fusion). Prey fragments of full length CryAB, CryAB D109A, CryAB D109H, CryAB R120G, and CryAB R157H were cloned in-frame with the Gal4 activation domain (AD) into plasmid pP7. Bait and prey constructs were transformed in the yeast haploid cells CG1945 (mata) and YHGX13 (Y187ade2-101::loxP-kanMX-loxP, matα) and diploid yeast cells were obtained using a mating protocol with both yeast strains. The interaction between SMAD and SMURF was used as positive control. As negative controls, all prey plasmids were tested with the empty vector (EV) pB66. Controls and interactions were tested in the form of streaks of three independent yeast clones for each control and interaction. Medium lacking tryptophan and leucine was used as a growth control and to verify the presence of the bait and prey plasmids. The selective medium without tryptophan, leucine, and histidine selected for the interaction between bait and prey and 0.05 mM 3-AT was added to select for interaction between bait and prey.

Zebrafish Congo red staining

Zebrafish embryos at 120 hpf from each condition were fixed for 3 h in 4% PFA (Merck KGaA, Darmastadt, Germany) and washed in PBS. Successively, embryos were permeabilized for 60 min with 10 μg/mL proteinase K in PBS and briefly re-fixed in 4% PFA in PBS for 20 min. After 3 PBS and 2 Milli-Q water washes, samples were incubated 1 hr in Congo red, followed by a Milli-Q wash of 10 min, a brief wash in a 0.036 M/L KOH solution in ETOH followed by 2 Milli-Q water washes. Samples were then analyzed using an Axiozoom.V16 fluorescence stereomicroscope equipped with Axiocamera 506 (Zeiss International, Oberkochen, Germany). The representative images were kindly taken by Prof A. Vettori's group at the CPT of the University of Verona with a confocal-Multiphoton Leica TCS SP5 AOBS with 20x objective (Leica Microsystem, Wetzlar, Germany).

Human biopsy histochemistry

For conventional histological and histochemical studies, consecutive or nonconsecutive 8-μm-thick cryosections were stained with haematoxylin and eosin (H&E), modified Gomori trichrome, adenosine triphosphatase (ATPase, pre-incubation at pH 4.3, 4.6 and 10.4), succinate dehydrogenase (SDH), cytochrome c oxidase (COX), reduced nicotinamide adenine dinucleotide (NADH), periodic acid-Schiff (PAS) with diastase digestion and Sudan black. Congo red staining was performed by 1 h incubation at room temperature in Congo red followed by consecutive washes in water, KOH solution (0.036 M/L) in 90% Ethanol, water and PBS. Congo red-stained sections were viewed under rhodamine fluorescence. Image acquisition was performed on Axioscope 5 equipped with Axiocam 208 color (Zeiss) and Axiolab fluorescence microscope equipped with AxioCam HRm (Zeiss).

QUANTIFICATION AND STATISTICAL ANALYSIS

Raw Data and Statistics Summary, related to the Main Figures.

Panel	Graph type	N value	Statistical test used	Precision	p-value
Figure 1C	Survival Curve	N≥50 for each genotype	Simple survival analysis (Kaplan-Meier)	Percent	p<0.0001
Figure 2C	Scatter bar plot	N≥10 for each genotype	Kruskal-Wallis test	Mean +/- SEM	ns, p<0.001, p<0.0001
Figure 2D	Scatter bar plot	N≥10 for each genotype	Kruskal-Wallis test	Mean +/- SEM	ns, p<0.01, p<0.001
Figure 2E	Column bar graph	N≥10 for each genotype	Mann-Whitney test	Mean +/- SEM	ns, p<0.0001
Figure 2G	Scatter bar plot	N=3 for each genotype	Kruskal-Wallis test	Mean +/- SD	ns, p<0.05, p<0.01
Figure 2H	Scatter bar plot	N=3 for each genotype	Kruskal-Wallis test	Mean +/- SD	ns, p<0.05
Figure 3A	Scatter plot	N≥10 for each genotype	Kruskal-Wallis test	Mean	ns, p<0.05, p<0.001, p<0.0001
Figure 3B	Scatter plot	N≥10 for each genotype	Kruskal-Wallis test	Mean	ns, p<0.05, p<0.01, p<0.0001
Figure 3C	Scatter plot	N≥10 for each genotype	Mann-Whitney test	Median	ns, p<0.05, p<0.0001
Figure 5C	Points & connecting line with error bars	N=6 for each genotype	Two way-ANOVA with Dunnett's multiple comparisons test	Mean and error +/- SD	p<0.01, p<0.001, p<0.0001
Figure 6B	Stacked bar	N≥29 for each genotype	Bonferroni's multiple comparison test	Mean +/- SEM	ns, p<0.001
Figure 6D	Stacked bar	N>20 for each genotype	Bonferroni's multiple comparison test	Mean +/- SEM	p<0.05, p<0.001
Figure 7H	Scatter bar plot	N=10 for each genotype	Mann-Whitney test	Mean +/- SD	p<0.0001

(*Continued on next page*)

Continued

Panel	Graph type	N value	Statistical test used	Precision	p-value
Figure 7I	Scatter bar plot	N=10 for each genotype	Mann-Whitney test	Mean +/- SD	ns, p<0.05, p<0.001
Figure 8C	Scatter bar plot	N=10 for each genotype	Mann-Whitney test	Mean +/- SD	p<0.0001
Figure 8D	Scatter bar plot	N=10 for each genotype	Mann-Whitney test	Mean +/- SD	ns, p<0.001
Figure 8G	Scatter bar plot	N=10 for each genotype	Mann-Whitney test	Mean +/- SD	p<0.01, p<0.001
Figure 8H	Scatter bar plot	N=10 for each genotype	Mann-Whitney test	Mean +/- SD	ns, p<0.05

Raw Data and Statistics Summary, related to the Supplementary Figures.

Panel	Graph type	N value	Statistical test used	Precision	p-value
Figure S1C	Scatter bar plot	$N \geq 80$ for each genotype	Kruskal-Wallis test	Mean ± SD	ns
Figure S1E	Scatter bar plot	N=3 for each genotype	Kruskal-Wallis test	Mean +/- SD	ns
Figure S2C	Scatter bar plot	N=3 for each genotype	Kruskal-Wallis test	Mean	p<0.05, p<0.01
Figure S2D	Scatter bar plot	N=3 for each genotype	Kruskal-Wallis test	Mean	p<0.05
Figure S3C	Scatter bar plot	N=3 for each genotype	Kruskal-Wallis test	Mean	ns
Figure S3D	Scatter bar plot	N=3 for each genotype	Kruskal-Wallis test	Mean	ns
Figure S4A	Point & connecting lines with error bars	N=3 for each genotype	Simple linear regression	Mean and error +/- SD	p<0.0001
Figure S4B	Point & connecting lines with error bars	N=3 for each genotype	Simple linear regression	Mean and error +/- SD	p<0.0001
Figure S5B	Scatter plot	N=10 for each genotype	Kruskal-Wallis test	Mean	ns
Figure S5C	Scatter plot	N=10 for each genotype	Kruskal-Wallis test	Mean	ns
Figure S7B	Column bar plot	N=2 for each interaction	N/A	Mean +/- SD	N/A